A kinematic calibration of the O-rich Mira variable period–age relation from *Gaia*

Hanyuan Zhang★ and Jason L. Sanders ★

Department of Physics and Astronomy, University College London, London WC1E 6BT, UK

ABSTRACT

Empirical and theoretical studies have demonstrated that the periods of Mira variable stars are related to their ages. This, together with their brightness in the infrared, makes them powerful probes of the formation and evolution of highly-extincted or distant parts of the Local Group. Here we utilize the *Gaia* DR3 catalogue of long-period variable candidates to calibrate the period–age relation of the Mira variables. Dynamical models are fitted to the O-rich Mira variable population across the extended solar neighbourhood and then the resulting solar neighbourhood period–kinematic relations are compared to external calibrations of the age–kinematic relations to derive a Mira variable period–age relation of $\tau \approx (6.9 \pm 0.3)\,\mathrm{Gyr}(1 + \tanh((330\,\mathrm{d} - P)/(400 \pm 90)\mathrm{d}))$. Our results compare well with previous calibrations using smaller data sets as well as the period–age properties of Local Group cluster members. This calibration opens the possibility of accurately characterizing the star formation and the impact of different evolutionary processes throughout the Local Group.

Key words: Galaxy: disc – Galaxy: evolution – Galaxy: kinematics and dynamics – stars: variables: general.

1 INTRODUCTION

In the study of the formation and evolution of the Milky Way, one crucial ingredient is accurate stellar ages (Freeman & Bland-Hawthorn 2002; Bland-Hawthorn & Gerhard 2016). With this information, we can begin disentangling the series of events that have led to the observed Milky Way today, as well as directly measure the dynamical restructuring of the Galaxy. However, despite their clear advantages in analysing the Galaxy, stellar ages are awkward quantities due to their indirect measurement only via stellar models. Many stellar age indicators exist (Soderblom 2010) which often provide different levels of accuracy for different stellar types and different stellar populations. With the availability of *Gaia* astrometry (Gaia Collaboration 2016, 2018) and complementary large-scale spectroscopic surveys (e.g. De Silva et al. 2015; Majewski et al. 2017), two methods applicable to large collections of stars are comparisons to isochrone models (e.g. Xiang et al. 2017; Sanders & Das 2018; Xiang & Rix 2022, which operates most successfully for subgiant stars that have recently turned off the main sequence), and indirect mass measurements of giant stars through spectroscopic measurements of the products of dredge-up episodes calibrated via asteroseismology (e.g. Masseron & Gilmore 2015; Martig et al. 2016).

Mira variables are high-amplitude thermally pulsing asymptotic giant branch (AGB) stars. Their study in the Large Magellanic Cloud (e.g. Glass & Evans 1981; Wood et al. 1999; Groenewegen 2004) demonstrated that they follow a tight period–luminosity relation (believed to be associated with fundamental mode pulsation) making them interesting tracers both for local Galactic and cosmological studies (Catchpole et al. 2016; Grady, Belokurov & Evans 2019,

2020; Huang et al. 2020). The chemistry of Mira variables is either oxygen or carbon-dominated depending on the C/O ratio (Höfner & Olofsson 2018), but O-rich Mira variables are significantly more common in the Milky Way and are found to follow tighter period–luminosity relations due potentially to less circumstellar dust (Ita & Matsunaga 2011). It has long been empirically known that groups of Mira variables binned by period show correlations between period and scaleheight/velocity dispersion (Merrill 1923; Feast 1963), which is typically interpreted as a correlation between the period and age of a Mira variable where the older stars have longer periods. This opens the possibility of using Mira variables as age indicators within the Galaxy and beyond (e.g. Grady, Belokurov & Evans 2020). A limited number of Mira variables in clusters also validate the period–age connection although confident assignment of membership has only been possible recently with *Gaia* data (Grady et al. 2019; Marigo et al. 2022). Although the period–age relation has been approximately calibrated empirically (Feast & Whitelock 2000b), relatively few theoretical models reproducing the behaviour exist (Wyatt & Cahn 1983; Eggen 1998; Trabucchi & Mowlavi 2022) and the lack of detailed reproduction of the period–luminosity relations of fundamental mode pulsation from theoretical models suggests the period–age relations still have some associated uncertainty and there is a need for accurate data-driven calibrations.

Encounters in the stellar discs of galaxies cause stellar populations to slowly kinematically heat giving rise to age–velocity dispersion relations (Wielen 1977) such as those suggested for Mira variable stars (Feast 1963). There are multiple suggested perturbers that give rise to disc heating including molecular clouds, spiral arms or merger events (Spitzer Lyman & Schwarzschild 1951, 1953; Barbanis & Woltjer 1967; Velazquez & White 1999; Hänninen & Flynn 2002; Aumer, Binney & Schönrich 2016) that likely have differing relative contributions across the Galactic disc (Mackereth et al. 2019). In the

★ E-mail: hz420@cam.ac.uk (HZ); jason.sanders@ucl.ac.uk (JLS)

solar neighbourhood, the stellar velocity dispersion is approximately a power law in age with exponent ∼0.3 for the radial dispersion and ∼0.5 for the vertical dispersion (Aumer & Binney 2009; Holmberg, Nordström & Andersen 2009; Sharma et al. 2021). A common picture (Binney & Tremaine 2008) for this behaviour is that the spiral arms are efficient in-plane heating sources giving rise to the increase in radial velocity dispersion and molecular clouds are efficient in converting this radial energy into vertical energy (Aumer et al. 2016). There is the further complication that the stellar populations could have been born hotter in the past, which could play a part in the observed correlations (Bird et al. 2021). Now with *Gaia* data, the age–velocity dispersion relations can be inspected across the Galactic disc (Sanders & Das 2018; Mackereth et al. 2019; Gaia Collaboration 2021; Sharma et al. 2021). For our purposes, the fact that correlations between age and kinematics exist is sufficient and we need not necessarily understand the underlying cause. In this way, kinematics can be used as an age proxy for groups of stars. Note that for this procedure to operate well, we are perhaps implicitly assuming that the kinematic–age relations are monotonic as evidenced in the solar neighbourhood (e.g. Holmberg et al. 2009).

With the publication of large catalogues of variable stars from *Gaia* with associated proper motions (Eyer et al. 2022), there is now the possibility of thorough characterizations of the dynamical properties of different families of Mira variable stars (Alvarez et al. 1997). Kinematic characterization then opens up the possibility of mutual age calibration of different age tracers. By assuming kinematics are solely a function of age, we can anchor different age indicators to each other by requiring they all reproduce the same age–kinematic relations (e.g Angus et al. 2015, 2020). In this way, we can characterize the Mira variable period–age relation. This simplifying assumption can be complicated by metallicity dependence, particularly if different tracers are biased toward different metallicity populations. The Mira variable stage occurs in stars of all metallicities although C-rich Mira variables are only formed through dredge-up in young, metal-poor stars (Boyer et al. 2013). This strategy of mutual age calibration via age–kinematic relations has been utilized successfully in the study of gyrochronology (Angus et al. 2015) and chromospheric activity in late-type stars (Wilson & Woolley 1970; West et al. 2015), and promises a route to the mutual calibration of all stellar age indicators.

In this work, we utilize the astrometry of the latest *Gaia* DR3 long-period variable candidate catalogue to characterize the kinematic behaviour of O-rich Mira variables separated by period and combine this information with literature age–velocity dispersion relations in the solar neighbourhood to characterize the period–age relation for O-rich Mira variable stars. In Section 2, we describe the data set we use focusing on the cuts required to isolate both O-rich AGB stars and those high-amplitude long-period variables that are likely Mira variables. In Section 3, we describe our modelling procedure and tests on mock data, before showing the results applied to data in Section 4 and the resulting period–age relation in Section 5. We critically discuss our approach and compare to other Mira variable period–age relations in Section 6 before summarizing our conclusions in Section 7.

2 THE *GAIA* DR3 O-RICH MIRA VARIABLE SAMPLE

We begin by describing how we form our O-rich Mira variable sample. It is important to note that our analysis relies on characterizing the velocity distributions at each Galactic location. In this way, considerations on the completeness of our sample are unimportant provided we do not perform any specific selections on the velocities

of the stars. Our primary objective with the selection is to form a low-contamination subset.

We use the long-period variable (LPV) candidate catalogue from *Gaia* DR3 (Gaia Collaboration 2016; Gaia Collaboration 2022b; Lebzelter et al. 2022). This catalogue has been constructed in a two-stage process – likely variable stars are identified by comparison to literature variable sources and reference non-variable *Gaia* sources, and then classified based on literature classifications and features including the Lomb–Scargle period, time summary statistics, colours, and parallax (Holl et al. 2018; Rimoldini et al. 2019, 2022). Stars classified as LPVs with G 5th−95th percentile greater than 0.1 mag and $G_{BP} − G_{RP} > 0.5$ (along with other less important cuts for our purposes) were further considered by the specific object study (SOS). Candidate LPVs from the SOS have published generalized Lomb–Scargle periods (and Fourier amplitudes) in *Gaia* DR3 if the period is greater than 35 d and shorter than the 34 month time series duration, the G-band signal to noise >15 and there is no correlation between the image determination parameters and the time series. Infrared photometric measurements were acquired from the 2MASS catalogue (Skrutskie et al. 2006) using the pre-computed cross-match provided on the *Gaia* archive. There are 1657 987 variable star observations in the *Gaia* DR3 LPV candidate SOS catalogue after the cross-match with 2MASS. We first remove stars without measured periods or without J and K_s photometric measurements which are needed for later selection pipelines. These requirements reduce the size of the sample to 387 419 objects.

To isolate a sample of likely Mira variables, we employ cuts in period and magnitude. We retain stars with $80 < \text{period}/\text{d} < 1000$ (Matsunaga et al. 2009) and in amplitude we employ a similar cut to Grady et al. (2019), which removes stars with amplitude < 0.5 mag (compared to Grady et al. 2019 cut at 0.43 mag). Here, amplitude is the G semi-amplitude computed from a Fourier fit. Note that around the problematic period of 190 d, the Fourier fit can significantly overestimate the amplitude of the LPVs leading to lower-amplitude semi-regular variable contaminants in a Mira variable selection. We remove stars with $170 < \text{period (d)} < 200$ and amplitude > 1.3, and $350 < \text{period (d)} < 400$ and amplitude > 1.6 to mitigate against this.

As highlighted by Mowlavi et al. (2018), young stellar objects (YSOs) can be a contaminant in the LPV processing as they have similar colours, amplitudes, and periods to LPVs. In the classification pipeline from Holl et al. (2018) and Rimoldini et al. (2019), the probability of the object being of the reported class, best_class_score, seems an effective indicator of YSOs. In Fig. 1, we show the colour–absolute magnitude diagram for our sample computed using a parallax adjusted by three times the parallax uncertainty. This gives the brightest possible magnitude for each star within the parallax uncertainties so any star consistent with being near the main sequence using this measure is likely a YSO. Many of these objects also have best_class_score < 0.8 so we choose to only consider stars with best_class_score > 0.8. From this series of cuts, we end up with 75 874 Mira variable star candidates.

2.1 O-rich/C-rich classification

LPVs can be either oxygen-rich or carbon-rich depending on the metallicity and the strength of the dredge-ups which is controlled by the initial mass (Höfner & Olofsson 2018). The O-rich stars follow a tighter period-luminosity relation (due to increased circumstellar dust in the C-rich stars, Ita & Matsunaga 2011) and are significantly more common in the Milky Way (with C-rich stars contributing more in the outer disc, Blanco, McCarthy & Blanco 1984; Ishihara et al.
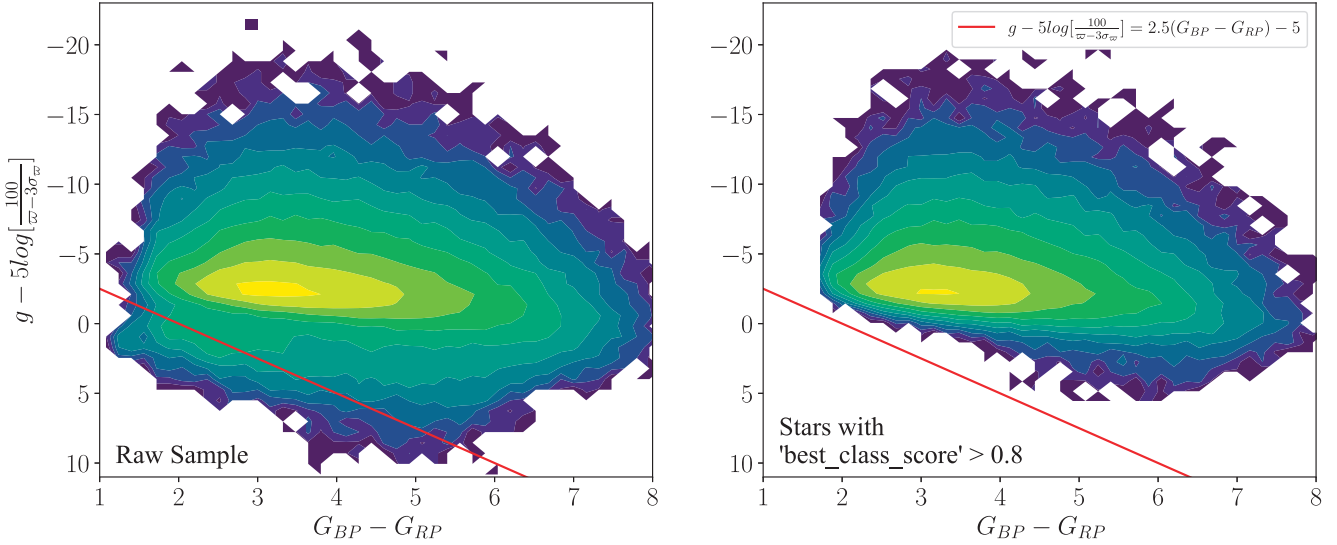
Figure 1. Colour–magnitude diagrams computed using a 3σ-adjusted parallax, $\varpi - 3\sigma_\varpi$. We define the region occupied by AGB stars as $G - 5\log_{10}(100/(\varpi - 3\sigma_\varpi)) < 2.5(G_{BP} - G_{RP}) - 5$: any star outside this is likely a YSO. The right-hand panel shows those only those stars with best_class_score > 0.8 which effectively removes any likely YSO contaminants.

2011). As shown by Lebzelter et al. (2022), the *Gaia* DR3 BP/RP (XP) spectra can be used to effectively separate O-rich and C-rich AGB stars due to the differing set of band heads and features in their spectra arising primarily from the TiO and CN absorption features. Sanders & Matsunaga (submitted) have provided an unsupervised classification approach for these spectra that effectively separates O-rich and C-rich LPV stars and performs better than the *Gaia* DR3 classifications for highly extincted sources. We adopt their classifications where *Gaia* DR3 XP spectra are available. Lebzelter et al. (2018) showed that, within the LMC, O-rich and C-rich Mira variables can be separated in the plane of $W_{BPRP} - W_{JK_s}$ versus K_s. Here, the two Wesenheit indices are $W_{BPRP} = G_{RP} - 1.3(G_{BP} - G_{RP})$ and $W_{JK_s} = K_s - 0.686(J - K_s)$. Although the boundary employed by Lebzelter et al. (2018) is slightly curved, we can employ a very similar cut to select O-rich Mira as $W_{BPRP} - W_{JK_s} < 1$. The left two panels of Fig. 2 show that this Wesenheit index difference against period for the selected Mira sample, whilst the right-hand panels are the period and distance percentage error of the O-rich Mira after further selections. The performance and purpose of these two cuts are very alike, but we employed both cuts here to maximally remove C-rich Mira contamination.

Aided by the XP spectrum classifications, we have found that O-rich and C-rich sources are separated in the period–amplitude plane and period–colour plane as shown in Fig. 3. Hence, we make a further two cuts to remove those C-rich Mira variables when an XP classification is not available: amplitude > $1.2 \log_{10}(\text{period/d}) - 2.22$; $G_{BP} - G_{RP} > 7\log_{10}(\text{period/d}) - 13.20$. The resulting number of O-rich Mira variable candidates was 46 107.

2.2 Assigning distances

The distance modulus, m, of O-rich Mira stars are estimated from the period–luminosity relation

$$M_{KJK} = \begin{cases} -7.53 - 4.05(\log_{10} P - 2.3), & \log_{10} P < 2.6, \\ -8.75 - 6.99(\log_{10} P - 2.6), & \log_{10} P \geq 2.6, \end{cases} \quad (1)$$

where P is the period in days and M_{KJK} the absolute Wesenheit magnitude, and the corresponding apparent Wesenheit magnitude
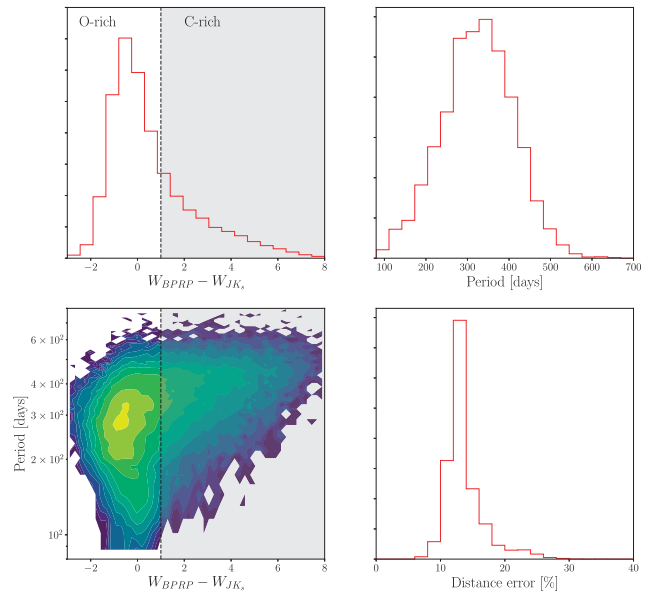

Figure 2. Properties of our O-rich Mira sample: the top left panel shows the distribution of the Wesenheit index difference from Lebzelter et al. (2018) used to separate O-rich and C-rich Mira. The lower left panel shows the distribution of this quantity versus period. The right two panels show the period and distance error for the O-rich Mira sample.

W_{KJK} is

$$W_{KJK} = K_s - 0.473(J - K_s). \quad (2)$$

The extinction coefficient is taken from Wang & Chen (2019). This extinction coefficient does not include the reddening caused by the circumstellar dust if its properties are different from the interstellar dust. Instead, because the period-luminosity relation is calibrated with respect to the O-rich Mira variables in the LMC, the reddening from circumstellar dust has already been considered in equation (1). The only caveat left is the potential difference in properties of the circumstellar dust between O-rich Mira variables in the LMC and the
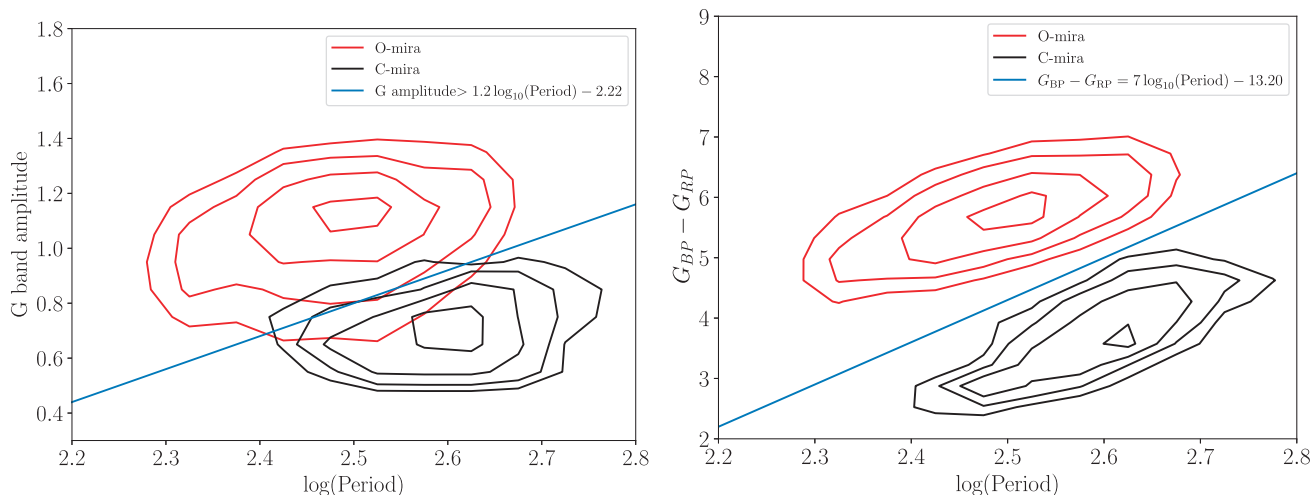
Figure 3. The contour plot of the C-rich (black) and O-rich (red) Mira variable population selected by their spectrum on period–amplitude plane and period–colour plane, respectively. Candidates below the blue line were removed from the sample.

Milky Way possibly arising due to the difference in metallicity. We consider this a minor effect in our analysis, particularly at shorter periods where significant circumstellar dust is uncommon (Ita & Matsunaga 2011).

The intrinsic scatter σ of the period-luminosity relation is

$$\sigma = \begin{cases} \sigma_{23} + m_{\sigma_1}(\log_{10} P - 2.3), & \log_{10} P < 2.6, \\ \sigma_{23} + 0.3m_{\sigma_1} + m_{\sigma_2}(\log_{10} P - 2.6), & \log_{10} P \geq 2.6, \end{cases} \quad (3)$$

where $\ln \sigma_{23} = -1.47$, $m_{\sigma_1} = 0.20$, and $m_{\sigma_2} = 0.89$. These relationships are taken from fits of the single-epoch 2MASS data for Mira variables in the LMC (Sanders, in preparation). The scatter is a combination of the single-epoch scatter and the intrinsic scatter due to variance in the population. Whitelock, Feast & Van Leeuwen (2008) has argued from a comparison of LMC Mira variables with local Mira variables with Hipparcos and VLBI parallaxes that the Mira variable period–luminosity relation is metallicity-independent, validating our use of the LMC relations for the Milky Way disc Mira variables. Sanders (in preparation) has shown that the W_{KJK} relations for the Milky Way are quite similar to the LMC relations. To compute the uncertainties in distance modulus, σ_m, we combine in quadrature the intrinsic scatter of the period–luminosity relation from equation (3) with the uncertainty propagated from the photometric and period measurement uncertainties. The typical period uncertainties give rise to a median scatter of 0.06 mag but the scatter arising from the single-epoch measurements is $\gtrsim 0.22$ mag. Note that the period uncertainties are only meaningful if the correct periodogram peak has been identified. In the case of aliases, the reported period can be formally inconsistent with the true period. Lebzelter et al. (2022) show the impact of aliasing is low. Additionally, in our modelling, we allow for the possibility of a star to be an 'outlier' which will capture any incorrectly assigned periods.

2.3 *Gaia* astrometric data quality

LPV stars are one of the most challenging regimes for the *Gaia* astrometric pipeline for a number of reasons. First, these sources are very red and *Gaia*'s image parameter determination is not well characterized for sources redder than $\nu_{eff} = 1.24 \, \mu m^{-1}$ (Rowell et al. 2021). Secondly, LPVs are variable whilst the current *Gaia* astrometric pipelines utilize a fixed colour in the modelling that could lead to systematics (Pourbaix et al. 2003). Finally

and possibly most importantly, LPVs can have radii of 1 AU or larger, and in the optical the photocentres wobble of the order of $\lesssim 10$ per cent the radius of the star (Chiavassa et al. 2011; Chiavassa, Freytag & Schultheis 2018). This additional photocentre wobble can lead to biases in the recovered astrometry (e.g. Andriantsaralaza et al. 2022) but as the motion is somewhat random and importantly not aligned in any special directions with respect to the parallactic and proper motion directions, particularly when averaging over many stars, the pre-dominant effect is that the reported astrometric uncertainties are underestimates of the true uncertainties.

Sanders (in preparation) has looked at the expected performance of *Gaia* on a set of modelled Mira variable stars and found that the parallax uncertainties must be inflated for higher parallax objects. This analysis agreed approximately with a full characterization of the period–luminosity relation and *Gaia* parallaxes for the Mira variable stars for which Sanders (in preparation) measured an inflation factor of $1 + \exp{[-(m - 8.5)/0.8]}$ for the parallax uncertainties. Here, we assume that the proper motion uncertainties must be inflated by the same factor (as validated by Sanders, in preparation). We do not consider the parallaxes in this work.

In addition to the inflation of the astrometric uncertainties on purely physical grounds, any mischaracterization of *Gaia*'s performance gives rise to misestimated astrometric uncertainties. Steps are taken to mitigate against this in the *Gaia* pipeline (Lindegren et al. 2012) but several studies have shown that problems likely still exist (e.g. El-Badry, Rix & Heintz 2021; Maíz Apellániz 2022). Again, this is particularly a concern for the redder sources due to the image parameter determination. Sanders (in preparation) has modelled the period–luminosity relation using the *Gaia* parallaxes including a flexible model for the factor by which *Gaia*'s parallax errors must be inflated. The model is two quadratics in G and ν_{eff} for the 5 – or 6 – parameter astrometric solutions respectively. We adopt their models for the W_{KJK} period–luminosity fits which typically require the parallax uncertainties to be inflated by a factor ~ 1.5. Although the inflation factor is appropriate for parallax errors, the astrometric modelling is a linear regression so underestimates in the output parameters reflect misestimates of the individual epoch astrometric (along-scan) measurements. It is therefore appropriate to assume all the astrometric uncertainties must be scaled in a similar way to the parallax uncertainties.
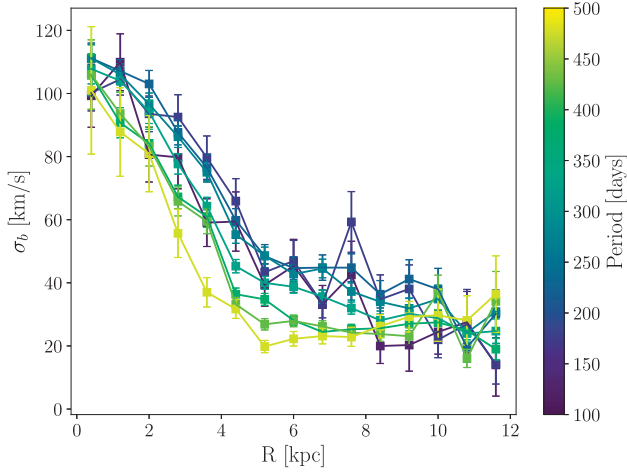
Figure 4. The transverse latitudinal velocity, v_b, dispersion profiles of O-rich Mira separated into different period bins. Stars in this figure are only from $|b| < 5°$, so v_b is approximately equal to the Galactic vertical velocity, or v_z, dispersion.

2.4 Final spatial cuts

We adopt a final series of spatial cuts to focus on Galactic disc members. We remove stars with $270° < \ell < 290°$, $-42° < b < -22°$, and $40 <$ heliocentric distance (kpc) < 60 to remove potential LMC candidates. As we only consider Mira variables from the Galactic disc, we removed possible bar-bulge contribution by cutting stars with $R < 5$ kpc, where R is the galactocentric radius. For the interest of kinematic modelling, we only looked at stars with heliocentric distance < 8 kpc and $R < 10$ kpc. Stars with $\sigma_m > 0.6$ are removed to avoid stars with extremely large spatial uncertainties. With all of the cuts described in this section, there remain 8 290 O-rich Mira variable star candidates in the sample.

3 KINEMATIC MODELLING USING DYNAMICAL MODELS

Due primarily to the specifics of the scanning law, *Gaia*'s detection of variable stars is a strong function of on-sky location and magnitude. This makes fitting density, or full dynamical, models to any *Gaia* variable data set difficult without a careful characterization of the selection function. Here, we employ a simpler approach by only considering the velocity, $\boldsymbol{v}$, distribution of our sample at each observed Galactic location, $\boldsymbol{x}$ i.e. $p(\boldsymbol{v}|\boldsymbol{x})$. Except in the most extreme cases, a Mira variable star will not fail to be in the catalogue as a result of its proper motion such that we can safely model the conditional distribution of the proper motions given position. We opt to work with full dynamical models $f(\boldsymbol{J})$ expressed as functions of the actions $\boldsymbol{J}$ due to their ability to capture the detailed shapes of the velocity distributions and their necessary linking of the radial and azimuthal velocity profiles.

In Fig. 4, we plot the latitudinal velocity dispersion profile for several period bins of the selected O-rich Mira as shown. A clear trend in period–dispersion relation is seen implying that the O-rich Mira variables follow a period–age relationship. In our modelling procedure, we will model populations of stars in period bins. Note that the periods are uncertain (as described in the previous section), but typically the uncertainty in the period is small (~ 10 d, except in the case of aliases) and mixing between bins is a small effect. Working with binned data significantly simplifies our procedure and

allows us to fully explore the kinematics with period rather than imposing some functional form. We discuss this latter possibility later.

For a given population of stars with similar periods, we wish to fit the probability distribution function $p(\boldsymbol{\mu}|\ell, b, m)$ where $\boldsymbol{\mu}$ is the proper motion vector, (ℓ, b) the Galactic coordinates and m the distance modulus (as described in the previous section). We begin by writing

$$p(\boldsymbol{\mu}|\ell, b, m) = \frac{p(\ell, b, m, \boldsymbol{\mu})}{p(\ell, b, m)} = \frac{\int \mathrm{d}v_{\|} \, p(\ell, b, m, \boldsymbol{\mu}, v_{\|})}{\int \mathrm{d}^2\boldsymbol{\mu} \, \mathrm{d}v_{\|} \, p(\ell, b, m, \boldsymbol{\mu}, v_{\|})}. \quad (4)$$

The proper motions and distance moduli are measured quantities with some associated uncertainties characterized by the proper motion covariance matrix $\boldsymbol{\Sigma}_\mu$ and the uncertainty in distance modulus σ_m. We, therefore, marginalize over the uncertainties by writing

$$p(\ell, b, m, \boldsymbol{\mu}, v_{\|})$$
$$= \int \mathrm{d}^2\boldsymbol{\mu}' \mathrm{d}m' \mathcal{N}(\boldsymbol{\mu}|\boldsymbol{\mu}', \boldsymbol{\Sigma}_\mu) \mathcal{N}(m|m', \sigma_m^2) p(\ell, b, m', \boldsymbol{\mu}', v_{\|}), \quad (5)$$

where $\mathcal{N}(x|\mu, \sigma^2)$ are Gaussians with mean μ and variance σ^2. We then relate the distribution in observable coordinates to the dynamical distribution function in actions as

$$p(\ell, b, m', \boldsymbol{\mu}', v_{\|}) = \left| \frac{\partial(\boldsymbol{J}, \boldsymbol{\theta})}{\partial(\ell, b, m, \boldsymbol{\mu}, v_{\|})} \right| f(\boldsymbol{J}) \propto s^5 \cos b \, f(\boldsymbol{J}), \quad (6)$$

where $\boldsymbol{J} = (J_r, J_\phi, J_z)$ is the set of actions corresponding to the observed 6d coordinate (with corresponding angle coordinates $\boldsymbol{\theta}$) and s is the distance corresponding to distance modulus m. Note the Jacobian between $(\boldsymbol{x}, \boldsymbol{v})$ and $(\boldsymbol{J}, \boldsymbol{\theta})$ is unity due to the canonical nature of the action-angle coordinates.

We choose $f(\boldsymbol{J})$ as a quasi-isothermal distribution function, which is suitable for warm discs (Binney 2010). We follow the implementation in AGAMA (Vasiliev 2019) which has a functional form given by

$$f(\boldsymbol{J}) = \frac{\tilde{\Sigma}\,\Omega}{2\pi^2 \kappa^2} \times \frac{\kappa}{\tilde{\sigma}_r^2} \exp\left(-\frac{\kappa J_r}{\tilde{\sigma}_r^2}\right) \times \frac{\nu}{\tilde{\sigma}_z^2} \exp\left(-\frac{\nu J_z}{\tilde{\sigma}_z^2}\right) \times B(J_\phi),$$

$$B(J_\phi) = \begin{cases} 1 & \text{if } J_\phi \geq 0, \\ \exp\left(\frac{2\Omega J_\phi}{\tilde{\sigma}_r^2}\right) & \text{if } J_\phi < 0, \end{cases}$$

$$\tilde{\Sigma}(R_c) \equiv \Sigma_0 \exp(-R_c/R_{\text{disc}}),$$

$$\tilde{\sigma}_r^2(R_c) \equiv \sigma_{r,0}^2 \exp(-2(R_c - R_0)/R_{\sigma,r}),$$

$$\tilde{\sigma}_z^2(R_c) \equiv \sigma_{z,0}^2 \exp(-2(R_c - R_0)/R_{\sigma,z}), \quad (7)$$

where R_c is the radius corresponding to a circular orbit of angular momentum $J_\phi \equiv L_z$ and (κ, Ω, ν) are the epicyclic frequencies at this angular momentum. This distribution function describes an approximately exponential disc in radius which is broadened/warmed vertically and radially by two exponential terms. There are five key free parameters for the model: (i) the scalelength of the disc, R_{disc}, (ii) the radial ($\sigma_{r,0}$) and vertical ($\sigma_{z,0}$) normalizations of the velocity dispersions at the Sun ($R = R_0$), and (iii) their corresponding scalelengths ($R_{\sigma,r}$ and $R_{\sigma,z}$). The actions are evaluated using the 'Stäckel fudge' algorithm described by Binney (2012), summarized and critically assessed against alternatives in Sanders & Binney (2016) and implemented in AGAMA (Vasiliev 2019). We adopt a fixed axisymmetric gravitational potential for the Galaxy from McMillan (2017). Fixing the potential could lead to sub-optimal model fits (as we will discuss later) but it significantly simplifies the computation and incorporates external constraints from the analysis of other data sets.

3.1 Computational considerations

The computational difficulty in evaluating equation (4) is computing the integrals efficiently. Here we use Monte Carlo integration. For the numerator, we generate a set of N samples for each star from the proper motion and distance modulus error ellipses. The unknown $v_\parallel$ is sampled from a probability distribution $G(v_\parallel|\ell, b, m, \boldsymbol{\mu})$ which is proportional to a quasi-isothermal distribution function with fixed parameters $f'(\boldsymbol{J})$ at a given $(\ell, b, m, \boldsymbol{\mu})$,

$$G(v_\parallel|\ell, b, m, \boldsymbol{\mu}) = \frac{p(\ell, b, m, \boldsymbol{\mu}, v_\parallel)}{\int \mathrm{d}v_\parallel \, p(\ell, b, m, \boldsymbol{\mu}, v_\parallel)} = A_{v_\parallel} f'(\boldsymbol{J}). \quad (8)$$

Samples are generated from this distribution using the inverse cumulative distribution. The value of $f'(\boldsymbol{J}_i)$ for each sample is stored to reweight the Monte Carlo sum. For the denominator, we sample $\boldsymbol{v} = (v_x, v_y, v_z)$ directly at a given observed position (ℓ, b, m) in a similar way to the numerator as

$$G(\boldsymbol{v}|\ell, b, m) = \frac{p(\ell, b, m, \boldsymbol{v})}{\int \mathrm{d}^3\boldsymbol{v} \, p(\ell, b, m, \boldsymbol{v})} = A_{\boldsymbol{v}} f'(\boldsymbol{J}), \quad (9)$$

from which samples are generated using Markov Chain Monte Carlo (MCMC; Foreman-Mackey et al. 2013), and once again $f'(\boldsymbol{J}_i)$ are stored. $A_{v_\parallel}$ and $A_{\boldsymbol{v}}$ defined in equations (8) and (9) are constant factors which can be computed for each individual star. Only the ratio of these two normalization factors is important:

$$A \equiv \frac{A_{\boldsymbol{v}}}{A_{v_\parallel}} = \frac{\int \mathrm{d}v_\parallel \, p(\ell, b, m, \boldsymbol{\mu}, v_\parallel)}{\int \mathrm{d}^3\boldsymbol{v} \, p(\ell, b, m, \boldsymbol{v})} = \frac{\int \mathrm{d}v_\parallel \, f'(\boldsymbol{J})}{\int \mathrm{d}^3\boldsymbol{v} \, f'(\boldsymbol{J})}. \quad (10)$$

A is evaluated using Monte Carlo integration: $v_\parallel$ and $\boldsymbol{v}$ are sampled from a Gaussian distribution centred on zero in the radial and vertical velocities, and on the rotation curve in the azimuthal velocity. As $f'(\boldsymbol{J})$ is fixed, A can be pre-computed once for each individual star to a desired accuracy. The $f'(\boldsymbol{J})$ we use throughout this paper has fixed parameters: $R_{\mathrm{disc}} = 2.5 \, \mathrm{kpc}$, $\sigma_{r,0} = 50 \, \mathrm{km \, s^{-1}}$, $\sigma_{z,0} = 50 \, \mathrm{km \, s^{-1}}$, $R_{\sigma,r} = 5.0 \, \mathrm{kpc}$, and $R_{\sigma,z} = 5.0 \, \mathrm{kpc}$. These parameters are chosen such that the distributions of the integration samples are typically broader than the modelled distributions to minimize bias in the Monte Carlo integration. Sampling from the distribution G, instead of a Gaussian distribution increases the computational efficiency by reducing the noise in the Monte Carlo integration for a fixed number of sampling. Now for each star, the integrals (up to a normalization constant) are given by

$$p(\ell, b, m, \boldsymbol{\mu}) \approx \frac{1}{N A_{v_\parallel}} \sum_i^{\substack{\text{errors in } m, \boldsymbol{\mu} \\ v_\parallel \text{ from } G(v_\parallel|\ldots)}} s_i^5 \cos b \frac{f(\boldsymbol{J}_i)}{f'(\boldsymbol{J}_i)}, \quad (11)$$

and

$$p(\ell, b, m) \approx \frac{1}{N A_{\boldsymbol{v}}} \sum_i^{\substack{\text{errors in } m \\ \boldsymbol{v} \text{ from } G(\boldsymbol{v}|\ldots)}} s_i^3 \cos b \frac{f(\boldsymbol{J}_i)}{f'(\boldsymbol{J}_i)}. \quad (12)$$

Note in the second expression we only have 3 powers of s as the integral has been rewritten in terms of the 3d space velocity $\boldsymbol{v}$ (as opposed to the observable space of proper motion and radial velocity). As we are using a fixed potential, we pre-compute $\boldsymbol{J}_i, R_{\mathrm{c}, i}$ and the epicyclic frequencies for all samples using the routines from Vasiliev (2019) and Bovy (2015).

3.2 Outlier component

Another complexity is to introduce an outlier distribution to overcome the contamination of samples by stars which are members of the halo, are possibly not Mira variable stars or have poorly measured periods. To do this, we assume that the velocity distribution of the contamination stars is described by a 3D spherically symmetric Gaussian distribution that is centred on Galactocentric $\boldsymbol{v} = \boldsymbol{0}$ with standard deviation in each dimension σ_v. Similar to the previous approach, we calculate the $p_{\mathrm{outlier}}(\boldsymbol{\mu}|\ell, b, m)$ using equations (4) and (5), but replacing $p(\ell, b, m', \boldsymbol{\mu}', v_\parallel)$ with $p_{\mathrm{outlier}}(\ell, b, m', \boldsymbol{\mu}', v_\parallel)$ which is chosen to be

$$p_{\mathrm{outlier}}(\ell, b, m', \boldsymbol{\mu}', v_\parallel) = s^5 \cos b \, \mathcal{N}(\boldsymbol{v}|\boldsymbol{0}, \sigma_v^2 \boldsymbol{I}) \mathcal{U}(x, y, z), \quad (13)$$

where $\mathcal{U}(x, y, z)$ is the uniform distribution in Galactocentric Cartesian spatial coordinates (x, y, z). For each star, $p_{\mathrm{outlier}}(\boldsymbol{\mu}|\ell, b, m)$ is evaluated numerically by

$$p_{\mathrm{outlier}}(\boldsymbol{\mu}|\ell, b, m) = \frac{\sum_i^{\text{errors in } m, \boldsymbol{\mu}} s_i^5 \mathcal{N}(s_i \boldsymbol{\mu}_i + \boldsymbol{v}_{t, \odot, i}|\boldsymbol{0}, \sigma_v^2 \boldsymbol{I})}{\sum_i^{\text{errors in } m} s_i^3}, \quad (14)$$

where $\boldsymbol{v}_{t, \odot}$ is the solar velocity in the Galactocentric frame projected in the plane perpendicular to the line of sight between the star and the Sun. To include this distribution in the log-likelihood, we rewrite the probability for each individual star as

$$p_{\mathrm{tot}, j} = (1 - \epsilon) p_j(\boldsymbol{\mu}|\ell, b, m) + \epsilon \, p_{\mathrm{outlier}, j}(\boldsymbol{\mu}|\ell, b, m). \quad (15)$$

Note with this definition, the outlier fraction at each spatial location, ϵ, is approximately constant. We choose the Gaussian because the contamination could come from a variety of sources, and the Gaussian distribution is a general, easily-computed way to characterize those sources.

3.3 Likelihood

We have now fully specified our model. The full log-likelihood for each population of stars is

$$\ln L = \sum_j^{\mathrm{stars}} \ln p_{\mathrm{tot}}(\boldsymbol{\mu}_j|\ell_j, b_j, m_j), \quad (16)$$

For each population of stars, we optimize the likelihood with respect to the five parameters of the quasi-isothermal (R_{disc}, $\sigma_{r, 0}$, $\sigma_{z, 0}$, $R_{\sigma, r}$, $R_{\sigma, z}$) and the two parameters of the outlier distribution (ϵ, σ_v). The log-likelihood is explored using MCMC performed with EMCEE (Foreman-Mackey et al. 2013). We adopt priors on the radial scale lengths as $R_{\mathrm{disc}} \sim \mathcal{N}(3.8 \, \mathrm{kpc}, (2 \, \mathrm{kpc})^2)$ and $R_{\sigma, r/z} \sim \mathcal{N}(4.5 \, \mathrm{kpc}, (3 \, \mathrm{kpc})^2)$ and a prior for velocity dispersion of the outlier component is a normal distribution $\sigma_v \sim \mathcal{N}(200 \, \mathrm{km \, s^{-1}}, (150 \, \mathrm{km \, s^{-1}})^2)$. The priors for the other three parameters are uniform: $\sigma_{r/z,0} \sim \mathcal{U}(0, 120 \, \mathrm{km \, s^{-1}})$ and $\epsilon \sim \mathcal{U}(0, 1)$.

A final step in our procedure is converting the modelled distribution function parameters to the physical measures of the velocity dispersion in the solar neighbourhood. It is these quantities we compare with previous characterizations of the age–velocity dispersion relation. For each set of (R_{disc}, $\sigma_{r, 0}$, $\sigma_{z, 0}$, $R_{\sigma, r}$, $R_{\sigma, z}$), we generate mock stars using the AGAMA DF sampling routines and fit an exponential profile $\sigma_i = \tilde{\sigma}_{i, 0} \exp[(R_0 - R)/\tilde{R}_{\sigma, i}]$ to the radial and vertical velocity dispersions binned in radius. The normalization $\tilde{\sigma}_{i, 0}$ and scalelength $\tilde{R}_{\sigma, i}$ give the physical velocity dispersion and its radial gradient in the solar neighbourhood.

3.4 Mock samples and validation

Given a fitted $f(\boldsymbol{J})$ model, we wish to draw mock samples to compare with the data and validate our fitting procedure. We use the AGAMA DF sampling routine to generate a large number of mock stars. For each generated mock star, we find the nearest observed star in our

data set in (R, z), place the mock star at the azimuth ϕ of the real star and transform the mock polar velocities to $\boldsymbol{\mu}$. This procedure exploits the axisymmetry of the models. We further scatter the proper motions and distance moduli of the mock stars by the corresponding uncertainties of the real stars. The previous Mira selection criteria in the heliocentric distance and R are also applied to the mock sample. Note this procedure produces a mock data set with each real star corresponding to multiple mock stars in proportion to the local stellar density at the location of the real star. This reduces the shot noise in our mock samples but means the mock sample has a different spatial density to the data. To reproduce the spatial distribution of the data set, we record the index of the closest matched real star for each mock star and then count the number of times that this real star is the closest match to any mock star. A weight is calculated for each mock star as the reciprocal of this number count. The weight will be used when we compare our fitted model to the data set. When directly comparing to a fitted data set, we further remove mock stars which do not reside within 100 pc of any real star (this requirement is not imposed on the mock test-set described below but makes little practical difference). Our procedure does not fully generate the data as we have not accounted for uncertainty in the data (R, z). However, it is sufficient for validation purposes.

We can use the generated mock observations to test the validity of our method. We generate a mock sample of 614 stars from $f(\boldsymbol{J})$ with known parameters chosen arbitrarily as $R_{\rm disc} = 3.8$ kpc, $\sigma_{r,0} = 45.0$ km s^{-1}, $\sigma_{z,0} = 35.0$ km s^{-1}, $R_{\sigma,r} = 4.5$ kpc, and $R_{\sigma,z} = 4.4$ kpc. We then replace velocities of 10 per cent of the generated data with $\boldsymbol{v}$ sampled from a spherically symmetric Gaussian $\mathcal{N}(\boldsymbol{v}|\boldsymbol{0}, (100\,{\rm km\,s^{-1}})^2\boldsymbol{I})$ which is the assumed velocity distribution of outlier stars. Stars sampled from the outlier distribution have a chance to be unbound from the potential, so after removing those unbound stars, the actual proportion of outlier stars can be smaller than 10 per cent, i.e. $\epsilon < 10$ per cent. Without those high-velocity stars in the mock sample, the velocity dispersion of the generated outlier stars is reduced so a fitted $\sigma_v < 100$ km s^{-1} is expected but the recovered parameters of the $f(\boldsymbol{J})$ model should be unbiased. The posteriors from the MCMC are shown in the low left of Fig. 5. The parameters $\sigma_{z,0}$ and $R_{\sigma_z,0}$ both deviate slightly from the default parameters but only around the 1σ level. In the upper right corner of Fig. 5, we convert each set of fitted parameters into the physical velocity dispersion profile parameters, $\widetilde{\sigma}_{i,0}$ and $\widetilde{R}_{\sigma,i}$. Although there are small differences in the distribution function parameters, the resulting physical velocity dispersions and scalelengths at the solar position are well recovered. We also produced the posterior of the same sample using the log-likelihood without the outlier distribution. The medians of the parameters are $R_{\rm disc} = 3.56$ kpc, $\sigma_{r,0} = 65.74$ km s^{-1}, $\sigma_{z,0} = 43.16$ km s^{-1}, $R_{\sigma,r} = 3.14$ kpc, and $R_{\sigma,z} = 2.48$ kpc. As expected, $\sigma_{r,0}$ and $\sigma_{z,0}$ are overestimated. This demonstrates that adding the outlier distribution is necessary when the contamination of the sample is significant.

4 VELOCITY DISPERSION OF O-RICH MIRA VARIABLE STARS IN DIFFERENT AGE BINS

To investigate the kinematic properties of the sample defined in Section 2, we put the O-rich Mira variables into period bins and treat stars in each bin as a sub-population drawn from the same DF. We choose the period bins to be wider than the typical uncertainties in the period measurements, and hence we neglect the period uncertainties that scatter stars from bin to bin (the impact of the period uncertainties on the distance uncertainties *have* been considered). The median of the period uncertainties is 11.6 and 7.1 d for those stars with periods

less than 300 d. We have also tried to bin stars with a wider period bin (50 d instead of 25), which gives very similar results to the presented binning strategy. The adopted priors on the radial scale-lengths are $R_{\rm disc} \sim \mathcal{N}(4\,{\rm kpc}, (3\,{\rm kpc})^2)$ and $R_{\sigma,r/z} \sim \mathcal{N}(10\,{\rm kpc}, (6\,{\rm kpc})^2)$, the prior for velocity dispersion of the outlier component is a normal distribution $\sigma_v \sim \mathcal{N}(100\,{\rm km\,s^{-1}}, (80\,{\rm km\,s^{-1}})^2)$ and the other priors are uniform as defined in the previous section. The posterior distributions for the fits of each period bin are given in the supplementary material and are summarized by the medians and percentiles in Table 1. The contamination fraction ϵ is generally small and σ_v generally large for all period bins. Table 2 reports the physical radial and vertical velocity dispersion normalization and scalelength in the solar neighbourhood, $\widetilde{\sigma}_{i,0}$ and $\widetilde{R}_{\sigma,i}$ respectively.

To verify the results of the MCMC fitting, we generate mock samples for the best-fitting parameters according to the procedure from Section 3.4, and we make use of the weights for the mock sample to compare the kinematics of the fitted model with the data set under the same spatial distribution. In Fig. 6, we have plotted the v_ℓ and v_b distributions of these mock samples compared to that of the observations, where $v_{\ell/b} = s \cdot \mu_{\ell/b}$. We have chosen to omit the lowest period bin (80–150 d) from this plot and in later plots and analysis because the contamination rate, ϵ is the highest among other period bins (see Table 1) and it is likely it does not follow the broad trend of increasing dispersion with decreasing period due to contamination from short-period-red stars as we will discuss in Section 6.3. For the displayed period bins, the mock samples generally agree with the observations. For some period bins, the shape of the observed v_b is sharper than the mock sample implying that our modelling has some caveats. Three reasons could lead to this: first, the assumed outlier distribution did not characterize the contamination accurately and underestimated the outlier star contribution consequently. Secondly, the period binning strategy needs to be improved. Bins at long periods cover Mira variables of a broader range of ages than the bins at short periods. Hence, if the younger stars in the period bin have much smaller velocity dispersion than the average of the bin, the sharper peak in observation would appear while the general shape of the overall distribution is still correct. Thirdly, the assumed functional form for the velocity dispersion parameters $\sigma_i = \sigma_{i,0}\exp(R_0 - R)/R_{\sigma,i}$ may be inappropriate. We illustrate this final possibility by plotting the radial profile of the longitudinal and latitudinal velocity dispersions σ_ℓ and σ_b in Fig. 7. For one or two period bins, the large R radial behaviour of σ_b is not completely in agreement with the observations. The σ_ℓ distribution is relatively more poorly fitted than the v_b distribution. Again, this could be due to the adopted form of the distribution function. However, apart from these very minor discrepancies, our modelling is in agreement with the observations. This is reinforced by the comparison of the v_ℓ and v_b distribution for $275 <$ Period/d < 300 in Fig. 8. The model is in good agreement with the observations. We will discuss further limitations of our approach in Section 6.

As noted previously, the spatial distribution of stars has not been considered in the modelling as it is subject to completeness effects arising from *Gaia*'s scanning law and the effects of extinction. As a result, the spatial distribution of the (unweighted) mock samples and the observations are in disagreement when the completeness of the data set is not considered. Our weighting of the mock samples reproduces the spatial distribution of the data enabling comparison of the kinematic fits as shown in Fig. 6, for example. When the weights are not considered, the mock sample distribution can be considered as the approximate underlying completeness-corrected distribution of the data (only up to a point as according to our procedure, where there is no data there will also be no mock stars). The weights are thus
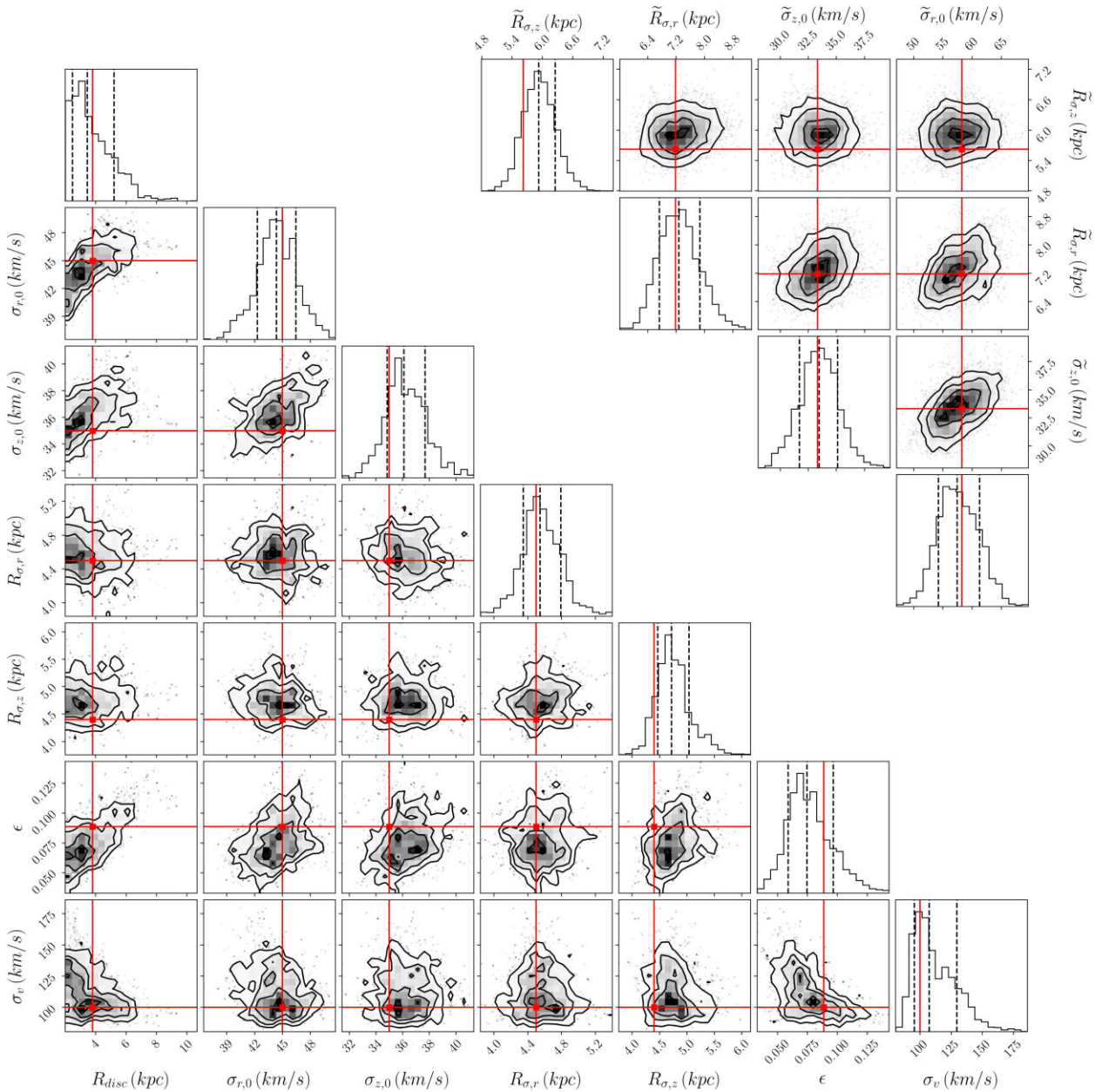
Figure 5. Results of fits on mock data: the lower left corner plot is the posterior of the fitting parameters from the test on mock data including an outlier distribution. The red lines are the parameters that generated the mock sample, and the black dashed lines are the 16th, 50th and 86th percentiles of the posterior, respectively. The upper right corner plot gives the posteriors of the physical velocity dispersion parameters corresponding to the sets of fitted parameters. The physical velocity dispersion parameters are propagated from the fitted parameters using the routine described in Section 4.

giving the proportion of stars at each x that have been observed. This is demonstrated in Fig. 9 by comparing the unweighted Galactic height distribution of the mock sample to the data set. Note that our procedure only gives access to the relative completeness so the histograms have been chosen to be normalized. The distributions of the data points are generally broader than the unweighted mock distributions, which we interpret as incompleteness in the data set towards the Galactic mid-plane, possibly arising from extinction. This interpretation of the unweighted mock samples assumes the distribution functions well describe the Milky Way sub-populations. We discuss the shortcomings of the approach later, but the good agreement in Fig. 9 also demonstrates that even without considering

incompleteness, the distribution functions do a good job of describing the data.

5 PERIOD–AGE RELATIONSHIP

With the dynamical distribution functions in each Mira variable period bin well characterized, we now turn to what this implies for the corresponding age of each period bin. To do this, we must adopt an age–velocity dispersion relation (AVR). We choose the AVR measured by Yu & Liu (2018) from LAMOST data of ∼3500 sub-giant/red giant stars. Yu & Liu (2018) characterized the velocity dispersions of their sample split into age bins using the entirety

Table 1. Distribution function parameter estimates for the Mira variable model fits. The left column gives the considered period bin and the other columns show the median and uncertainties estimated from the 16th and 84th percentiles.

Period range (d)	Mean period (d)	Number of stars	R_{disc} (kpc)	$\sigma_{r,0}$ (km s^{-1})	$\sigma_{z,0}$ (km s^{-1})	$R_{\sigma,r}$ (kpc)	$R_{\sigma,z}$ (kpc)	ϵ	σ_v (km s^{-1})
80–150	126.4	230	$3.55^{+2.40}_{-1.19}$	$48.05^{+6.17}_{-4.83}$	$30.45^{+2.14}_{-2.01}$	$8.32^{+3.29}_{-1.64}$	$9.65^{+2.28}_{-2.41}$	$0.06^{+0.02}_{-0.02}$	$151.49^{+30.72}_{-22.91}$
150–200	179.3	430	$3.56^{+1.27}_{-0.74}$	$40.59^{+3.06}_{-3.26}$	$41.07^{+3.62}_{-3.46}$	$3.54^{+0.25}_{-0.19}$	$6.47^{+1.14}_{-1.10}$	$0.02^{+0.02}_{-0.02}$	$105.58^{+61.84}_{-40.22}$
200–225	212.8	442	$5.11^{+1.00}_{-1.35}$	$53.14^{+5.51}_{-5.39}$	$51.72^{+3.39}_{-2.89}$	$5.05^{+1.19}_{-0.60}$	$9.52^{+2.06}_{-1.94}$	$0.01^{+0.04}_{-0.01}$	$46.46^{+111.19}_{-21.72}$
225–250	237.7	494	$3.79^{+1.43}_{-0.82}$	$37.66^{+2.66}_{-2.18}$	$55.99^{+3.74}_{-4.19}$	$3.97^{+0.32}_{-0.31}$	$10.36^{+2.89}_{-2.19}$	$0.01^{+0.01}_{-0.01}$	$78.35^{+71.38}_{-36.07}$
250–275	263.3	708	$3.53^{+1.95}_{-0.91}$	$52.38^{+3.59}_{-3.72}$	$42.22^{+1.83}_{-2.10}$	$12.16^{+3.37}_{-2.72}$	$7.41^{+1.30}_{-0.92}$	$0.03^{+0.02}_{-0.01}$	$79.23^{+28.35}_{-12.22}$
275–300	287.2	909	$4.47^{+1.55}_{-0.98}$	$51.79^{+2.49}_{-2.11}$	$39.57^{+2.00}_{-1.75}$	$13.57^{+3.08}_{-2.17}$	$7.24^{+1.27}_{-0.87}$	$0.02^{+0.01}_{-0.01}$	$104.36^{+22.33}_{-15.63}$
300–325	313.0	907	$2.72^{+0.71}_{-0.58}$	$46.46^{+2.04}_{-2.18}$	$34.53^{+1.90}_{-1.72}$	$11.68^{+2.13}_{-1.49}$	$8.12^{+1.50}_{-1.15}$	$0.00^{+0.01}_{-0.00}$	$109.87^{+45.84}_{-36.79}$
325–350	337.7	970	$2.49^{+0.67}_{-0.47}$	$43.15^{+1.68}_{-1.75}$	$32.94^{+1.34}_{-1.18}$	$12.10^{+2.50}_{-1.54}$	$9.08^{+1.55}_{-1.17}$	$0.01^{+0.01}_{-0.00}$	$114.63^{+37.64}_{-21.27}$
350–375	362.3	861	$5.29^{+1.78}_{-1.38}$	$42.44^{+1.82}_{-1.78}$	$28.84^{+1.26}_{-1.38}$	$13.52^{+4.08}_{-2.42}$	$11.35^{+2.55}_{-2.39}$	$0.01^{+0.01}_{-0.01}$	$79.10^{+79.99}_{-45.18}$
375–400	387.3	784	$4.69^{+2.07}_{-1.41}$	$42.33^{+2.26}_{-1.62}$	$23.89^{+1.54}_{-1.49}$	$12.01^{+3.08}_{-1.96}$	$7.89^{+2.12}_{-1.27}$	$0.01^{+0.01}_{-0.01}$	$79.19^{+48.55}_{-32.91}$
400–450	422.5	1015	$2.87^{+1.40}_{-0.69}$	$41.45^{+1.81}_{-1.61}$	$25.77^{+0.86}_{-1.04}$	$14.43^{+3.11}_{-2.01}$	$13.69^{+2.48}_{-1.58}$	$0.00^{+0.01}_{-0.00}$	$88.41^{+66.37}_{-43.88}$
450–500	470.9	396	$3.18^{+2.57}_{-1.28}$	$37.42^{+1.90}_{-2.27}$	$19.56^{+1.59}_{-1.71}$	$13.22^{+2.70}_{-2.64}$	$15.03^{+2.70}_{-4.03}$	$0.04^{+0.02}_{-0.02}$	$82.44^{+21.10}_{-18.52}$
500–600	527.5	144	$4.68^{+2.68}_{-2.10}$	$34.27^{+3.22}_{-2.85}$	$16.85^{+1.92}_{-2.41}$	$11.45^{+3.82}_{-3.06}$	$11.34^{+5.52}_{-3.99}$	$0.02^{+0.03}_{-0.01}$	$121.84^{+69.88}_{-44.77}$

Table 2. Solar neighbourhood velocity dispersions and local spatial gradients of the velocity dispersions for the Mira variable fits. The age estimations are also provided, where τ_r is the age estimation from the radial velocity dispersion while τ_z is that from the vertical velocity dispersion.

Period (d)	$\widetilde{\sigma}_{r,0}$ (km s^{-1})	$\widetilde{\sigma}_{z,0}$ (km s^{-1})	$\widetilde{R}_{\sigma,r}$ (kpc)	$\widetilde{R}_{\sigma,z}$ (kpc)	τ_r (Gyr)	τ_z (Gyr)
80–150	$49.83^{4.39}_{3.78}$	$24.59^{1.47}_{2.13}$	$10.54^{3.94}_{2.13}$	$9.04^{1.64}_{1.64}$	$8.57^{+1.13}_{-0.34}$	$6.34^{+0.36}_{-0.34}$
150–200	$67.20^{4.70}_{4.20}$	$34.44^{1.86}_{1.43}$	$6.88^{0.62}_{0.61}$	$7.46^{0.85}_{0.92}$	$10.82^{+0.56}_{-0.52}$	$8.07^{+0.82}_{-0.75}$
200–225	$62.96^{2.99}_{3.11}$	$38.24^{1.55}_{1.56}$	$7.92^{1.47}_{0.91}$	$9.37^{1.48}_{1.27}$	$10.41^{+0.45}_{-0.45}$	$9.34^{+0.64}_{-0.66}$
225–250	$52.83^{3.00}_{3.20}$	$40.24^{1.67}_{1.78}$	$6.16^{0.53}_{0.53}$	$10.10^{1.66}_{1.42}$	$9.25^{+0.73}_{-0.89}$	$9.72^{+0.61}_{-0.67}$
250–275	$51.90^{2.48}_{2.29}$	$32.92^{1.14}_{1.16}$	$15.31^{4.51}_{3.61}$	$7.78^{0.94}_{0.77}$	$9.09^{+0.72}_{-0.78}$	$7.58^{+0.60}_{-0.55}$
275–300	$50.54^{2.07}_{1.91}$	$31.08^{1.21}_{1.08}$	$16.61^{4.20}_{2.97}$	$7.54^{1.05}_{0.76}$	$8.75^{+0.78}_{-0.70}$	$7.25^{+0.52}_{-0.44}$
300–325	$46.67^{1.73}_{1.72}$	$27.57^{1.11}_{1.01}$	$14.35^{2.78}_{2.08}$	$8.05^{1.15}_{0.87}$	$7.80^{+0.55}_{-0.57}$	$6.77^{+0.35}_{-0.35}$
325–350	$43.27^{1.50}_{1.54}$	$26.27^{0.86}_{0.88}$	$14.41^{3.15}_{2.00}$	$8.66^{1.10}_{0.91}$	$7.01^{+0.59}_{-0.54}$	$6.61^{+0.34}_{-0.34}$
350–375	$41.74^{1.67}_{1.69}$	$23.11^{0.89}_{0.93}$	$15.35^{4.79}_{2.96}$	$10.24^{1.74}_{1.75}$	$6.66^{+0.52}_{-0.49}$	$6.20^{+0.33}_{-0.30}$
375–400	$41.98^{1.84}_{1.47}$	$20.02^{1.00}_{0.94}$	$13.73^{3.78}_{2.23}$	$7.82^{1.65}_{1.12}$	$6.67^{+0.51}_{-0.49}$	$5.66^{+0.34}_{-0.32}$
400–450	$41.08^{1.58}_{1.50}$	$20.92^{0.71}_{0.76}$	$16.45^{3.56}_{2.46}$	$11.61^{1.65}_{1.17}$	$6.43^{+0.47}_{-0.43}$	$5.86^{+0.31}_{-0.31}$
450–500	$37.21^{1.87}_{2.03}$	$16.46^{1.21}_{1.16}$	$14.60^{3.38}_{2.91}$	$12.58^{3.00}_{2.60}$	$5.52^{+0.57}_{-0.57}$	$4.60^{+0.61}_{-0.96}$
500–600	$34.24^{2.99}_{2.78}$	$14.65^{1.34}_{1.85}$	$12.44^{4.03}_{3.23}$	$10.46^{3.60}_{3.11}$	$4.50^{+0.86}_{-1.12}$	$3.62^{+0.76}_{-1.05}$
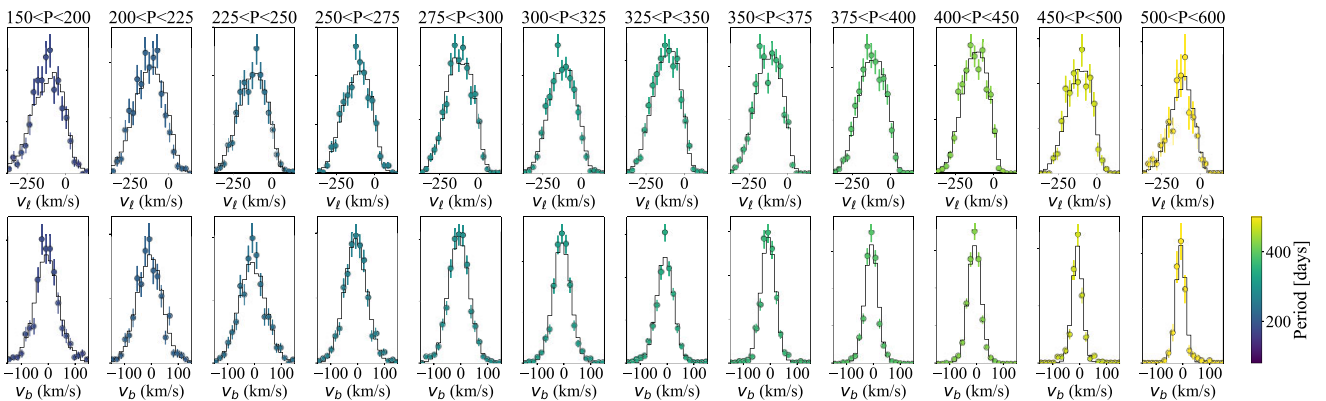
Figure 6. Velocity histograms for O-rich Mira variables separated by period (as given in days above each column). The top panels show v_ℓ and bottom v_b. The points are data and black lines the models.
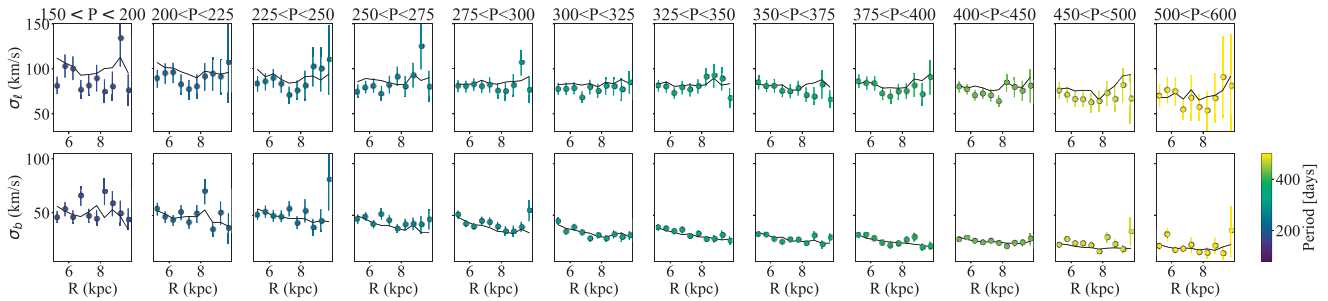
Figure 7. Velocity dispersion profiles as a function of Galactocentric radius for O-rich Mira variables separated by period (as given in days above each column). The top panels show longitudinal, ℓ, and bottom latitudinal, b. The points are data and black lines the models.
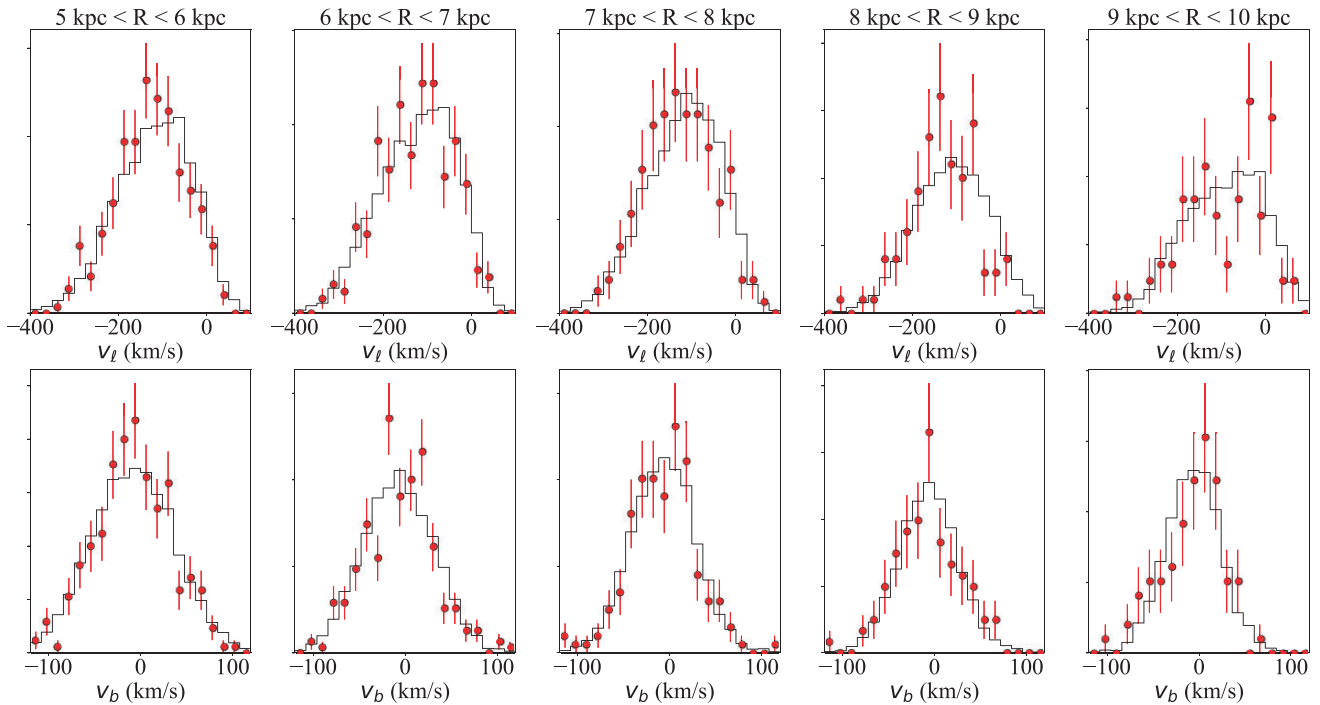

Figure 8. Velocity histograms for O-rich Mira variables with periods in the range 275–300 d separated into bins of Galactocentric radius (as given above each column). The top panels show the longitudinal velocity v_ℓ and the bottom the latitudinal velocity, v_b. The red points are data and the black lines are the models.
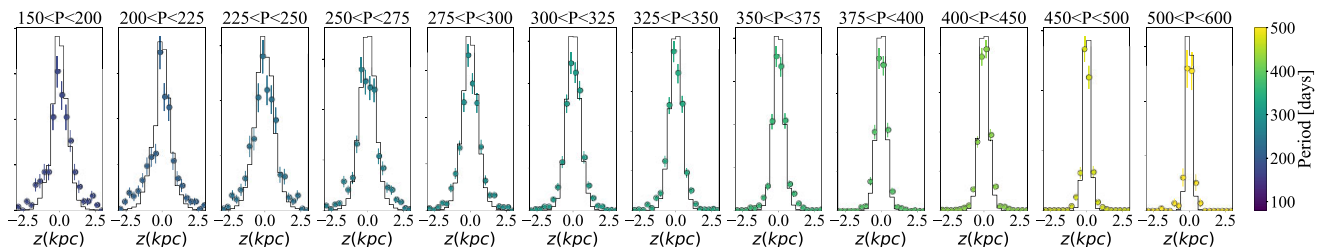
Figure 9. Vertical density distribution profile for O-rich Mira variables separated by period bins (as given in days above each panel). Each panel shows the data set (points) compared to the unweighted distribution of mock samples (black lines). All histograms are normalized, and subplots do not share the same y-axis. The discrepancy between the distributions is a reflection of the completeness of the data set.

of their data set and also for two sets split by Galactic height: $|z| < 0.27$ kpc and $|z| > 0.27$ kpc. The ages of stars in Yu & Liu (2018) were estimated by comparing the stellar parameters ([Fe/H], T_{eff}, $\log g$) measured by LAMOST to a grid of isochrone models. Age estimates were found by marginalizing the likelihood over initial mass and absolute magnitude. The AVRs were produced by further

binning stars in their sample by age. This procedure accounts for uncertainties arising from the velocities but *not* the ages. We discuss the impact of this later.

We estimate the corresponding AVR of our sample by averaging the two $|z|$-separated AVRs in Yu & Liu (2018) weighted by the number of stars in our sample that are above and below $|z| = 0.27$ kpc
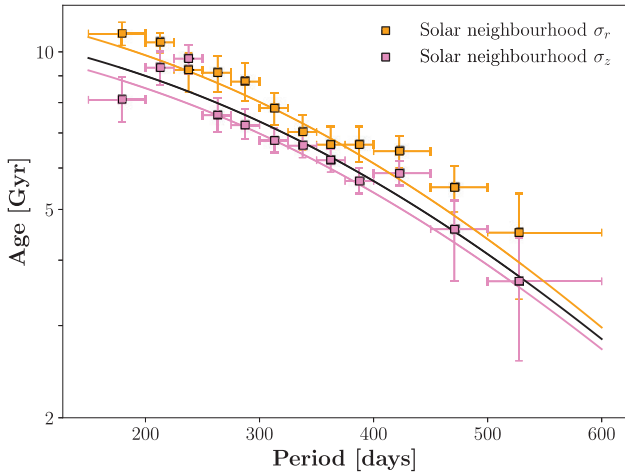
Figure 10. The calibrated age–period relationship of the O-rich Mira variables. The orange and violet points are the velocity dispersion from the kinematic modelling. The orange, purple, and black lines are the fitted period–age relations using radial, vertical velocity dispersions, and two together, respectively, with fitted parameters given in Table 3.

in each bin. Consequently, the final AVR was slightly different for each bin. At low ages, the corresponding AVR is not monotonic due in part to uncertainties and the low numbers of stars in some low-age bins. Thus, we remove points in the AVR if the age is less than that of the previous age bin so that we could interpolate a monotonic AVR to find an age at each radial and vertical dispersion, $\widetilde{\sigma}_{r,0}$ and $\widetilde{\sigma}_{z,0}$. The uncertainty is again propagated using Monte Carlo samples. The final calibrated age–period relationship is shown in Fig. 10.

Yu & Liu (2018) discussed that the uncertainties in the estimated ages of stars would broaden the measured AVR. Liu et al. (2015) argued that the age estimation method used in Yu & Liu (2018) could have uncertainties at the 30 per cent level which propagate from the uncertainties of the LAMOST stellar parameters. Here, we will discuss how much this effect would affect the period–age relationship. We generate 500 000 stars with uniformly distributed ages and assign each star a radial and vertical velocity from a Gaussian distribution centred at 0 with standard deviations of σ_r and σ_z calculated from the AVR. Then, the ages of the stars are scattered by (10, 20, 30) per cent uncertainties. We then bin the stars with the scattered age and calculate the measured radial and vertical velocity dispersion. The ratio of the measured to actual velocity dispersion for the AVR is given in Fig. 11, where the left-hand and right-hand panels are made for the AVR of $|z| < 0.27$ kpc and $|z| > 0.27$ kpc, respectively. We divide this ratio by the corresponding velocity dispersions in the AVR as a correction. In Fig. 12 we show the period–age relations calibrated using AVRs with different levels of age uncertainty. We see that with 30 per cent uncertainty in AVR the maximum correction could be up to 20 per cent in age as calibrated from $\sigma_{R,0}$ and 34 per cent from $\sigma_{z,0}$.

We have also considered other recent AVR calibrations available in the literature. For example, Sharma et al. (2021) have provided a fit of the radial and vertical dispersions in a separable form in terms of the age, angular momentum, metallicity, and Galactic height. Their relations produce significantly smaller dispersions at fixed age such that the derived period–age relation will assign significantly larger ages at fixed period which in the extreme can be $\gg 14$ Gyr. We are therefore inclined to use the Yu & Liu (2018) relations and the applicability of the Sharma et al. (2021) relations merits further investigation.

6 DISCUSSION

We now turn to the interpretation and understanding of our results, in particular concentrating on the comparison with previous period–age estimates for Mira variable stars and possible future model improvements.

6.1 Comparison with Mira variable cluster members and previous results

In Fig. 10, we display a series of period–age indicators of Mira variable stars. The age–kinematic method for period–age calibration has been utilized by Feast, Whitelock & Menzies (2006), Feast (2009), and Feast & Whitelock (2014). Feast & Whitelock (2000b) demonstrated that Mira variables in the solar neighbourhood exhibited clear correlations between period and kinematics. These have been translated approximately into period–age measurements using results from the solar neighbourhood in the cited works. However, it should be said that all of the quoted results are only approximate due to the absence of robust age–kinematics calibrations.

Mira variables in clusters give a more direct measurement of the period–age relation than the indirect method using the age–kinematics calibrations. Unfortunately, there are comparatively few cluster Mira variables. Those in globular clusters have been studied by Sloan et al. (2010) whilst those with good evidence of Milky Way open cluster membership from *Gaia* have been studied by Marigo et al. (2022). There are also many candidates for LMC cluster membership as studied by Grady et al. (2019). However, membership of an LMC cluster is difficult to discern purely from projected coordinates (as used by Grady et al. 2019) and proper motion data. We compile Mira variable globular cluster members using the globular cluster variable star compilation from Clement et al. (2001). We consider all stars flagged as 'M' or 'M?', and not flagged as a likely field star ('f' or 'f?'). Furthermore, if available, we ensure the *Gaia* DR3 proper motion is within 3σ of the measured cluster mean proper motion from Vasiliev & Baumgardt (2021). Here, σ is a quadrature sum of the measurement uncertainty and the central velocity dispersion. We complement with ages primarily from VandenBerg et al. (2013) and Dotter et al. (2010), and from Beaulieu et al. (2001) for NGC 6553, Geisler et al. (2007) for Terzan 7, Ortolani et al. (1999) for Terzan 1, Marín-Franch et al. (2009) for NGC 6441 and Forbes & Bridges (2010) for NGC 6356, NGC 6388, NGC 6642, and NGC 6760. Terzan 5 has evidence of multiple star formation events (Ferraro et al. 2016) so we assign stars with periods <400 d an age of 12 Gyr and longer-period stars an age of 4.5 Gyr. There is a carbon-rich Mira variable in the old globular cluster Lyngå 7 that has been suggested as a product of binary evolution (Feast, Menzies & Whitelock 2013). However, its *Gaia* DR3 proper motion is not consistent with being a cluster member. Its radial velocity is perfectly consistent so one possibility is that the *Gaia* measurement is spurious. This seems quite likely as there are two nearby *Gaia* DR3 sources with only two-parameter astrometric solutions suggesting contamination in the Lyngå 7 C-rich Mira variable measurement.

For Mira variable open cluster members, we use the compilation from Marigo et al. (2022) adopting their measured periods and the cluster ages from Cantat-Gaudin et al. (2020). Marigo et al. (2022) identify some cluster members on the fundamental period–luminosity relation followed by Mira variable stars but with too low an amplitude for traditional Mira variable classification. We consider all stars that Marigo et al. (2022) identify as fundamental pulsators
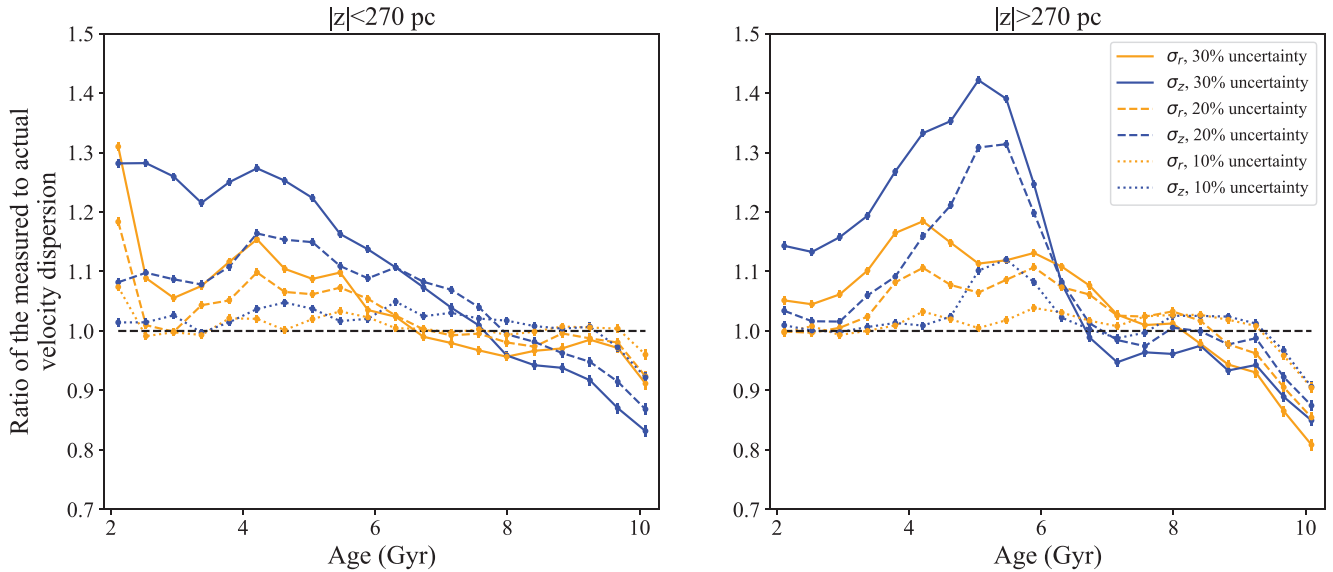
Figure 11. The ratio of the age–velocity dispersion relation broadened by different age uncertainties (10, 20, and 30 per cent denoted by dotted, dashed, and solid) relative to the 'true' age–velocity dispersion relation without age uncertainties. The left-hand panel shows results for the $|z| < 0.27$ kpc AVR from Yu & Liu (2018) and the right-hand panel their age–velocity dispersion relation for $|z| > 0.27$ kpc. Yellow lines correspond to σ_r and blue σ_z.
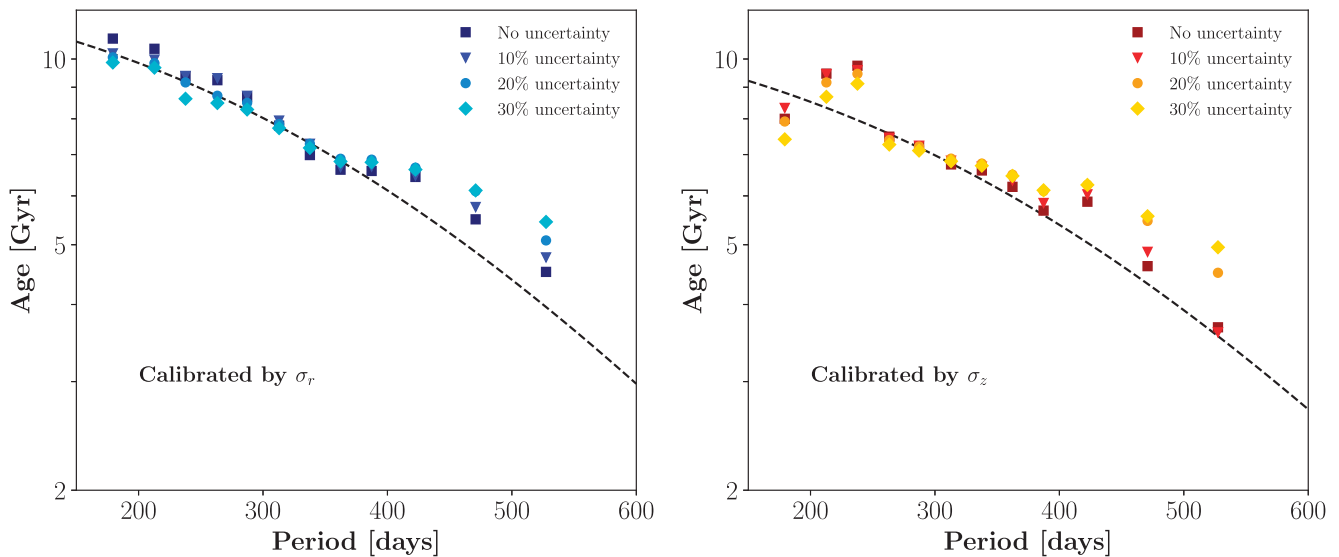
Figure 12. The calibrated period–age relationship using age–velocity dispersion relations broadened by different age uncertainties (as labelled in the legend). The relation calibrated by $\widetilde{\sigma}_{r,0}$ is shown in the left-hand panel while $\widetilde{\sigma}_{z,0}$ is on the right. The error bars are not shown in this figure. The black dashed lines in both panels are the fitted period–age relations shown by the orange and pink lines in Fig. 10, respectively.

and with *G* band amplitudes greater than 0.865 mag (Grady et al. 2019) estimated from the photometric uncertainties. There are two such stars with are both C-rich.

Finally, we consider possible LMC and SMC cluster members from the *Gaia* DR3 LPV candidate catalogue. We combine the list of cluster ages from Baumgardt et al. (2013) and Bonatto & Bica (2010). To limit contaminants, we conservatively find all *Gaia* DR3 LPV candidates within one cluster radius as determined by Bica et al. (2008) (adopting the median cluster radius of 0.45 arcmin when a radius is not available). We further limit to those with proper motions within 3σ of $(\mu_{\alpha}*, \mu_{\delta}) = (1.910, 0.229)$mas yr^{-1} (Kallivayalil et al. 2013) where σ is the quadrature sum of the uncertainties and 100 km s^{-1} at the distance of the LMC, and those with distances

between 30 and 70 kpc as determined from equation (1). We isolate Mira variables by restricting to stars with *G* amplitudes > 0.865 mag as determined by the *G* photometric uncertainties and the Fourier light-curve fits. This results in 4 high-confidence LMC cluster members.

The described combination of cluster measurements is shown in Fig. 13. We see in general the good agreement between the results derived from the age–kinematic relation and the cluster members. There are some globular cluster members with longer periods but higher ages (most notably the 312 d period Mira in NGC 5927 which has an age of 12.25 Gyr from Dotter et al. 2010 and 10.75 Gyr from VandenBerg et al. 2013). This may reflect metallicity dependence in the period–age relation or these
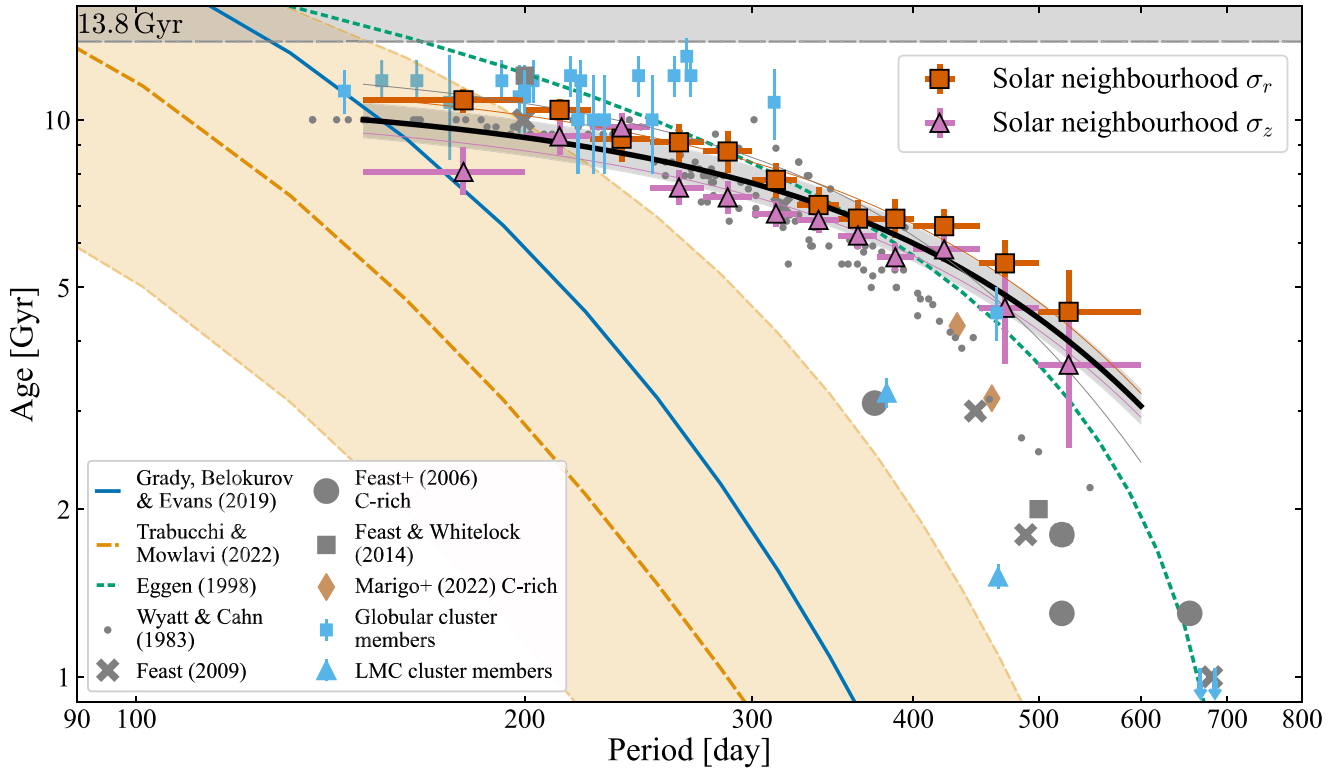
Figure 13. Comparison of the derived period–age relations with other literature results. The orange squares and pink triangles show our Mira variable period–age measurements from Table 2. The small grey points are from the models of Wyatt & Cahn (1983), the green short-dashed line from the model of Eggen (1998) and the orange long-dashed line from the model of Trabucchi & Mowlavi (2022, along with the associated scatter shown by the shaded region). The light blue squares are Mira variable globular cluster members from Clement et al. (2001), the brown diamonds C-rich Mira variable open cluster members from Marigo et al. (2022) and the light-blue triangles LMC cluster members. The solid blue line is a fit from Grady et al. (2019) to a broader sample of LMC cluster members. The grey points are period–age estimates for disc populations from Feast et al. (2006), Feast (2009), and Feast & Whitelock (2014). The black line is the joint fit of our results and the globular cluster members from Table 3 and the thinner orange, pink, and grey lines show the other three fits from that same table.

could be the results of binary evolution in these clusters producing slightly more massive AGB stars than expected at fixed age.

There are several theoretical period–age relations from the literature. The earliest of these are the results from Wyatt & Cahn (1983) who found ages for local Mira variable stars via main-sequence mass estimates derived from models of Mira variables as fundamental pulsators which were fitted to optical and infrared photometry and periods. Eggen (1998) similarly provided a theoretically motivated period–age relation by supposing fundamental Mira-like pulsations occur once a star of a given mass (age) reaches some critical radius. Most recently, Trabucchi & Mowlavi (2022) have used theoretical models to produce period–age calibrations for O-rich and C-rich Mira variable stars. They highlighted one expectation of the models is a large spread of age at fixed period. Furthermore, their period–age relations agreed very well with the cluster member measurements mostly compiled by Grady et al. (2019). However, as we have hinted at above, there is perhaps good reason to believe that the LMC cluster members are quite a contaminated set and that LMC field stars coincident on the sky with the clusters are likely to be incorrectly identified as cluster members. The field stars will typically be older than the cluster members, having already left their parent clusters, and so these contaminants will act to decrease the typical age at fixed period. It could be that there is an additional variable controlling the period–age relation that produces the discrepancy between the LMC clusters and the local age–kinematic relations. The spread in models from Trabucchi & Mowlavi (2022) is almost consistent with

the measurements made here. However, the globular clusters suggest any metallicity dependence would go the other way. Furthermore, binary evolution produces higher periods at fixed age so would not explain the discrepancy.

A further supporting piece of evidence for the age–period relation we have derived here is the properties of the LMC population as a whole and the Galactic bulge sample. In both sets, there are stars with $\sim$ 500–600 d periods. From our calibrations, these stars are $\sim$ 3–4 Gyr old. The LMC has a tail towards longer periods consistent with even more recent star formation. The Galactic bulge is primarily considered as an old population (Zoccali et al. 2003) although there has been significant evidence that there are intermediate-age populations as young as 3 Gyr (Bensby et al. 2013; Nataf 2016; Bensby et al. 2017). Our calibration is entirely consistent with these results. A lower age–period relation would mean a significant population of stars in the Galactic bulge with $\lesssim$ 1 Gyr old populations although again we should stress the expected spread in ages at each period could still produce some consistency in the results.

6.2 A parametric period–age relation

Our fitting has provided the approximate ages of O-rich Mira variable populations in a series of period bins. It is more convenient to work with an analytical relation that approximately fits the results. The flexible form

$$\tau = \tau_0 \frac{1}{2} \left(1 + \tanh \left[\frac{330 - P(\mathrm{ds})}{P_s} \right] \right), \tag{17}$$

Table 3. Functional form for the period–age relation fitted to our results. We adopt the form $\tau = (\tau_0/2)(1 + \tanh((330 - P(\mathrm{d}))/P_s)$ with a fractional age uncertainty of f_τ.

Subset	τ_0	P_s	$\ln f_\tau$
σ_r	14.9 ± 0.7	389 ± 77	-6.70 ± 0.01
σ_z	13.0 ± 0.5	404 ± 111	-5.71 ± 0.03
Both	13.7 ± 0.6	401 ± 88	-2.63 ± 0.04
With GC	14.7 ± 0.7	308 ± 54	-2.17 ± 0.04

provides an approximate fit to the data. We take the data reported in Table 2 and fit equation (17) allowing for an additional fractional scatter in the ages of f_τ such that the age errors are $\sqrt{\sigma_\tau^2 + f_\tau^2 \tau^2}$. (τ_0, P_s, f_τ) are given logarithmic flat priors and we sample using EMCEE (Foreman-Mackey et al. 2013). We fit for σ_r and σ_z both separately and jointly and report the results in Table 3. Although the dispersion parameters are derived from the same model fit, the corner plots in the supplementary material demonstrate the parameter constraints are uncorrelated for nearly all period bins validating treating the results in this way. We also perform a joint fit of the dispersion results together with the globular cluster member compilation described in the previous section, again reporting the results in Table 3. All four sets of results are quite consistent with σ_z-only fits producing the lowest age at fixed period and the combination with the globular clusters producing the highest. As expected, the scatter is largest for the combined fit with the globular clusters but nevertheless, the scatter is only around 10 per cent in age.

6.3 Model limitations and future improvements

Before concluding, we will discuss some of the limitations of our modelling and possible improvements that could be adopted in future analyses.

6.3.1 Binning in period

We have opted to bin our data in period and analyse each period bin independently. This is a valid approach as the period uncertainties are typically quite small: the median period uncertainty is 11.6 and 7.1 d for period < 300 d. Hence, our strategy is valid for most of the period bins considered. A further generalization is to express the models in terms of the period as a continuous subpopulation label. We then have to introduce hyper-parametrizations for the parameters in $f(\boldsymbol{J})$ to express $f(\boldsymbol{J}|P)$. The integrals would involve an additional integral over the label P and we would have a weighting of the populations $f(P)$ (which if we are considering periods as proxies for age is akin to a star formation rate and could be an exponential in age, for example). The advantage of this approach is a more principled accounting of the period uncertainties as well as providing a route to consider the spread in age (kinematics) at each period that might arise from helium flashes, hot-bottom burning or the presence of short-period red stars. The downside of such an approach is that we would have to fit a parametrized form for the parameters as a function of P making the models significantly more complicated and potentially producing biased by our choice of functional form.

6.3.2 Velocity dispersion profile

We have here adopted a simple pure exponential decay for the velocity dispersion of each period bin. This form gives a good fit of the models to the data, particularly as we have chosen a rather limited Galactocentric radial range. It has been suggested that the velocity dispersion in the outer disc flattens or even increases with radius (Sanders & Das 2018; Mackereth et al. 2019). For example, Sharma et al. (2021) argues that the pure exponential decay of the velocity dispersions is not well motivated by the data, which shows signs of a rising dispersion beyond the solar radius. To incorporate this possibility, one possible change is to modify $\tilde{\sigma}_i(R_c)$ as

$$\tilde{\sigma}_i(R_c) \equiv \sigma_{i,0}(\exp[-(R_c - R_0)/R_{\sigma,i}] + \alpha_i(R_i/R_0)^2)/(1 + \alpha_i), \quad (18)$$

with the additional fitting parameters α_i to match the flattening/upturning dispersion profiles in the outer disc as suggested by Sharma et al. (2021). This may be a necessary enhancement when modelling the data beyond the extended solar neighbourhood. For example, if one were to consider investigating possible metallicity dependence of the period–age relation. However, such an enhancement does not seem necessary for our data.

6.3.3 Limitations of equilibrium axisymmetric distribution function approach

It is reassuring to note that the age estimates from the radial and vertical dispersions separately give very similar results for the period–age relation of the O-rich Mira variables. However, the relation derived from the radial dispersion is consistently higher than that derived from the vertical dispersion. We have seen how our dynamical models capture well both the longitudinal and latitudinal velocity distributions of the sample but typically the latitudinal distributions are better modelled suggesting our results are more reliable for the period–age relation derived from σ_z. This occasional mismatch of the longitudinal dispersion in Fig. 7 could be a shortcoming of the use of a quasi-isothermal distribution function. There are other action-based disc models available in the literature (e.g. Binney & Vasiliev 2023) which could be explored. As mentioned previously, using a dynamical distribution function simply incorporates the required asymmetry in the azimuthal component as well as necessarily linking together the radial and azimuthal dispersions due to the requirement of dynamical equilibrium. There could also be inconsistencies arising from this assumption of equilibrium as it is known that the Galactic disc shows non-equilibrium structure at the 5–10 per cent level. Any inflation of the velocity dispersion as a result of this is not a concern as we have anchored to tracers that will also display this inflation. The assumption of axisymmetry could also be giving rise to similar variations. We are using the velocity dispersion at the solar radius from a range of different azimuths but if the velocity dispersion is varying significantly with azimuth (e.g. *Gaia* Collaboration 2022), the comparison between our sample and the age–velocity dispersion results from Yu & Liu (2018) may be inappropriate. Furthermore, our model has assumed a fixed Milky Way potential from McMillan (2017). Whilst this potential captures many of the global features of the Milky Way, it may not in detail be appropriate across the entirety of the Galactic disc region considered here. In the wrong potential, it may be very difficult to fully match the full velocity distribution of the data at every spatial location. Reasonable variations of the potential will likely inflate the uncertainties in our derived parameters. We should also note that although we have inflated the *Gaia* astrometric uncertainties in our analysis to reflect shortcomings of the current *Gaia* data processing, it is likely that future *Gaia* data releases will improve the uncertainty estimates providing a better handle on the underlying dispersions of the disc populations. This may decrease the dispersion for the youngest populations (e.g. the 500–600-d period bin) but the dispersions of the oldest populations are very insensitive to the uncertainties so we believe our measurements are reliable.

6.3.4 SP-red stars

We found the stars in our lowest considered period bin (80–150 d) have significantly lower dispersions and hence lower ages than the neighbouring 150–200 d bin (see Table 1). This bucks the broad trend seen in e.g. Fig. 13 and for this reason, as well as the fact that this bin requires the largest outlier fraction of all modelled bins, we decided to neglect these results in our period–age relation fits. Feast & Whitelock (2000b) found a similar effect from Hipparcos data that they attribute to short-period(SP)-red stars which contaminate the short-period end and are kinematically more similar to the longer-period Mira variables. It is not clear exactly what the origin of these stars is and they could represent a different evolutionary stage to the bulk Mira variable population. Feast & Whitelock (2000b) hypothesize they could be stars on their way to becoming longer-period Mira variables or temporarily dimmed during their helium-shell flash cycle (Trabucchi et al. 2017). From *Gaia*–2MASS colour–colour diagrams, we did not clearly identify a distinct population of SP-red-like stars in the short-period bin but it is likely they are present and potentially also more weakly contaminating the 150–200 d bin which also shows a slightly lower σ_z than perhaps expected. It is known that Mira variables in globular clusters follow a period–metallicity relation with shorter-period stars more prevalent in metal-poor clusters (Feast & Whitelock 2000a). This then suggests that the shortest period bin we considered has significant contamination from more metal-poor objects and is not representative of the broader solar neighbourhood samples used to calibrate the period–age relations. However, it is then surprising that a more metal-poor population would have a lower than expected dispersion as in both *in situ* and accreted scenarios the opposite is likely the case. More generally, our methodology could be impacted by metallicity effects. We have already limited to O-rich Mira variables which should preferentially remove metal-poor stars. Further investigation is required to separate out the degeneracies between period, age and metallicity, and a possible avenue is to consider the variation of kinematics with unextincted colour as a metallicity proxy (e.g. Alvarez et al. 1997).

6.3.5 Hot-bottom burning

From equation (1), the slope of the period–luminosity relation changes after Period(days) > 400. This hints that our O-rich Mira variable star sample with periods above 400 d is a mixture of hot-bottom burning (HBB) stars and low-mass fundamental pulsators right at the end of their lifetime (Whitelock et al. 2003; Trabucchi et al. 2019). The balance of these two kinematically distinct populations depends on the star formation history (e.g. the HBB population would be reduced if there is no recent star formation). Hence, as we are measuring the average age at a fixed period, our result is somewhat related to the star formation history of the Milky Way. This mixing of HBB stars likely also broadens the period–age relation for period (d) > 400 (as it perhaps does the period–luminosity relation e.g. Ita & Matsunaga 2011), and it might address the small discrepancy between our relation and the literature results shown in Fig. 13. We hypothesize that the period–age relation is more universal and reliable for periods under 400 d.

6.3.6 C-rich stars

Finally, a further direction is to consider the C-rich Mira variables from *Gaia*. C-rich Mira variables also follow period–luminosity relations that are typically broader than that for the O-rich Mira variables due to circumstellar dust (Ita & Matsunaga 2011). They

also appear to trace period–age relations (e.g. Feast et al. 2006, and evidenced in Fig. 13). Typically they are less abundant in the Galaxy than the O-rich counterparts (Ishihara et al. 2011) but importantly are biased towards younger ages (and lower metallicities, e.g. Boyer et al. 2013) so present a route to better constraining the longer-period end of the Mira variable period–age relation.

7 CONCLUSIONS

We have used the *Gaia* DR3 long-period variable candidate catalogue to produce a calibration of the Mira variable period–age relation. Using a carefully selected population of likely O-rich Mira variable stars, we have fitted a series of action-based dynamical models to the stars separated by period. We have found very good model fits for the velocity distributions of our sample from which we have derived period–kinematic relations for the solar neighbourhood. Comparison with an age–velocity dispersion relation for sub-giant/red giant stars in the solar neighbourhood has allowed us to provide a calibration of the Mira variable period–age relation.

Our derived relation agrees well with previous literature approaches using a similar methodology and with the members of clusters with known ages. Some theoretical models agree well with the derived relation but more recent calibrations appear to be consistently younger at fixed period than our relations suggest. Consideration of the age distribution of Mira variable stars in the Galactic bar-bulge produces a consistent picture with other bar-bulge age tracers using our relation.

This new period–age relation opens the possibility of inspecting the star formation history and evolutionary properties of distant and/or highly-extincted regions of our Galaxy and the Local Group. Mira variables are some of the brightest stars in an intermediate-age population, their infrared brightness makes them ideal tracers of dusty environments, and their high amplitude and long periods mean they suffer low contamination. For these reasons, in the era of *JWST*, Mira variables will provide us with a new window of the evolution of the Universe.

DATA AVAILABILITY

All data utilized in this work are in the public domain. In the supplementary material, we provide corner plots showing the posterior distributions of the dynamical model parameters for each period bin.

REFERENCES

Alvarez R., Mennessier M. O., Barthes D., Luri X., Mattei J. A., 1997, A&A, 327, 656

Andriantsaralaza M., Ramstedt S., Vlemmings W. H. T., De Beck E., 2022, A&A, 667, A74

Angus R. et al., 2020, AJ, 160, 90

Angus R., Aigrain S., Foreman-Mackey D., McQuillan A., 2015, MNRAS, 450, 1787

Astropy Collaboration, 2013, A&A, 558, A33

Aumer M., Binney J. J., 2009, MNRAS, 397, 1286

Aumer M., Binney J., Schönrich R., 2016, MNRAS, 462, 1697

Barbanis B., Woltjer L., 1967, ApJ, 150, 461

Baumgardt H., Parmentier G., Anders P., Grebel E. K., 2013, MNRAS, 430, 676

Beaulieu S. F., Gilmore G., Elson R. A. W., Johnson R. A., Santiago B., Sigurdsson S., Tanvir N., 2001, AJ, 121, 2618

Bensby T. et al., 2013, A&A, 549, A147

Bensby T. et al., 2017, A&A, 605, A89

Bica E., Bonatto C., Dutra C. M., Santos J. F. C., 2008, MNRAS, 389, 678

Binney J., 2010, MNRAS, 401, 2318

Binney J., 2012, MNRAS, 426, 1324

Binney J., Tremaine S., 2008, Galactic Dynamics: Second Edition. Princeton University Press, Princeton

Binney J., Vasiliev E., 2023, MNRAS, 520, 1832

Bird J. C., Loebman S. R., Weinberg D. H., Brooks A. M., Quinn T. R., Christensen C. R., 2021, MNRAS, 503, 1815

Blanco V. M., McCarthy M. F., Blanco B. M., 1984, AJ, 89, 636

Bland-Hawthorn J., Gerhard O., 2016, ARA&A, 54, 529

Bonatto C., Bica E., 2010, MNRAS, 403, 996

Bovy J., 2015, ApJS, 216, 29

Boyer M. L. et al., 2013, ApJ, 774, 83

Cantat-Gaudin T. et al., 2020, A&A, 640, A1

Catchpole R. M., Whitelock P. A., Feast M. W., Hughes S. M. G., Irwin M., Alard C., 2016, MNRAS, 455, 2216

Chiavassa A. et al., 2011, A&A, 528, A120

Chiavassa A., Freytag B., Schultheis M., 2018, A&A, 617, L1

Clement C. M. et al., 2001, AJ, 122, 2587

De Silva G. M. et al., 2015, MNRAS, 449, 2604

Dotter A. et al., 2010, ApJ, 708, 698

Eggen O. J., 1998, AJ, 115, 2435

El-Badry K., Rix H.-W., Heintz T. M., 2021, MNRAS, 506, 2269

Eyer L. et al., 2022, preprint (arXiv:2206.06416)

Feast M. W., 1963, MNRAS, 125, 367

Feast M. W., 2009, in Ueta T., Matsunaga N., Ita Y., eds, AGB Stars and Related Phenomena. National Astronomical Observatory of Japan, Mitaka, Tokyo, Japan, p. 48

Feast M. W., Menzies J. W., Whitelock P. A., 2013, MNRAS, 428, L36

Feast M. W., Whitelock P. A., 2000b, MNRAS, 317, 460

Feast M. W., Whitelock P. A., Menzies J. W., 2006, MNRAS, 369, 791

Feast M., Whitelock P. A., 2014, in Feltzing S., Zhao G., Walton N. A., Whitelock P., eds, Proc. IAU Symp. 298, Setting the scene for Gaia and LAMOST. Kluwer, Dordrecht, p. 40

Feast M., Whitelock P., 2000a, in Matteucci F., Giovannelli F., eds, Astrophysics and Space Science Library Vol. 255, The Evolution of the Milky Way: Stars Versus Clusters. Springer-Verlag, Berlin, p. 229

Ferraro F. R., Massari D., Dalessandro E., Lanzoni B., Origlia L., Rich R. M., Mucciarelli A., 2016, ApJ, 828, 75

Forbes D. A., Bridges T., 2010, MNRAS, 404, 1203

Foreman-Mackey D., 2016, J. Open Source Softw., 1, 24

Foreman-Mackey D., Hogg D. W., Lang D., Goodman J., 2013, PASP, 125, 306

Freeman K., Bland-Hawthorn J., 2002, ARA&A, 40, 487

Gaia Collaboration, 2016, A&A, 595, A1

Gaia Collaboration, 2018, A&A, 616, A1

Gaia Collaboration, 2021, A&A, 649, A8

Gaia Collaboration, 2022a, preprint (arXiv:2206.06207)

Gaia Collaboration, 2022b, preprint (arXiv:2208.00211)

Geisler D., Wallerstein G., Smith V. V., Casetti-Dinescu D. I., 2007, PASP, 119, 939

Glass I. S., Evans T. L., 1981, Nature, 291, 303

Grady J., Belokurov V., Evans N. W., 2019, MNRAS, 483, 3022

Grady J., Belokurov V., Evans N. W., 2020, MNRAS, 492, 3128

Groenewegen M. A. T., 2004, A&A, 425, 595

Hänninen J., Flynn C., 2002, MNRAS, 337, 731

Höfner S., Olofsson H., 2018, A&A Rev., 26, 1

Holl B. et al., 2018, A&A, 618, A30

Holmberg J., Nordström B., Andersen J., 2009, A&A, 501, 941

Huang C. D. et al., 2020, ApJ, 889, 5

Hunter J. D., 2007, Comput. Sci. Eng., 9, 90

Ishihara D., Kaneda H., Onaka T., Ita Y., Matsuura M., Matsunaga N., 2011, A&A, 534, A79

Ita Y., Matsunaga N., 2011, MNRAS, 412, 2345

Kallivayalil N., van der Marel R. P., Besla G., Anderson J., Alcock C., 2013, ApJ, 764, 161

Lebzelter T. et al., 2022, preprint (arXiv:2206.05745)

Lebzelter T., Mowlavi N., Marigo P., Pastorelli G., Trabucchi M., Wood P. R., Lecoeur-Taïbi I., 2018, A&A, 616, L13

Lindegren L., Lammers U., Hobbs D., O'Mullane W., Bastian U., Hernández J., 2012, A&A, 538, A78

Liu C. et al., 2015, preprint (arXiv:1510.06123)

Mackereth J. T. et al., 2019, MNRAS, 489, 176

Maíz Apellániz J., 2022, A&A, 657, A130

Majewski S. R. et al., 2017, AJ, 154, 94

Marigo P. et al., 2022, ApJS, 258, 43

Marín-Franch A. et al., 2009, ApJ, 694, 1498

Martig M. et al., 2016, MNRAS, 456, 3655

Masseron T., Gilmore G., 2015, MNRAS, 453, 1855

Matsunaga N., Kawadu T., Nishiyama S., Nagayama T., Hatano H., Tamura M., Glass I. S., Nagata T., 2009, MNRAS, 399, 1709

McKinney W., 2010, in van der Walt S., Millman J., eds, Proceedings of the 9th Python in Science Conference. p. 56

McMillan P. J., 2017, MNRAS, 465, 76

Merrill P. W., 1923, ApJ, 58, 215

Mowlavi N. et al., 2018, A&A, 618, A58

Nataf D. M., 2016, PASA, 33, e023

Ortolani S., Barbuy B., Bica E., Renzini A., Marconi G., Gilmozzi R., 1999, A&A, 350, 840

Pourbaix D., Platais I., Detournay S., Jorissen A., Knapp G., Makarov V. V., 2003, A&A, 399, 1167

Price-Whelan A. M. et al., 2018, AJ, 156, 123

Rimoldini L. et al., 2019, A&A, 625, A97

Rimoldini L. et al., 2022, Gaia DR3 Documentation Chapter 10: Variability, Gaia DR3 Documentation, European Space Agency; Gaia Data Processing and Analysis Consortium. p. 10

Rowell N. et al., 2021, A&A, 649, A11

Sanders J. L., Binney J., 2016, MNRAS, 457, 2107

Sanders J. L., Das P., 2018, MNRAS, 481, 4093

Santos J. F. C.J., Piatti A. E., 2004, A&A, 428, 79

Sharma S. et al., 2021, MNRAS, 506, 1761

Skrutskie M. F. et al., 2006, AJ, 131, 1163

Sloan G. C. et al., 2010, ApJ, 719, 1274

Soderblom D. R., 2010, ARA&A, 48, 581

Spitzer Lyman J., Schwarzschild M., 1951, ApJ, 114, 385

Spitzer Lyman J., Schwarzschild M., 1953, ApJ, 118, 106

Trabucchi M., Mowlavi N., 2022, A&A, 658, L1

Trabucchi M., Wood P. R., Montalbán J., Marigo P., Pastorelli G., Girardi L., 2017, ApJ, 847, 139

Trabucchi M., Wood P. R., Montalbán J., Marigo P., Pastorelli G., Girardi L., 2019, MNRAS, 482, 929

van der Walt S., Colbert S. C., Varoquaux G., 2011, Comput. Sci. Eng., 13, 22

VandenBerg D. A., Brogaard K., Leaman R., Casagrande L., 2013, ApJ, 775, 134

Vasiliev E., 2019, MNRAS, 482, 1525

Vasiliev E., Baumgardt H., 2021, MNRAS, 505, 5978

Velazquez H., White S. D. M., 1999, MNRAS, 304, 254

Virtanen P. et al., 2020, Nat. Methods, 17, 261

Wang S., Chen X., 2019, ApJ, 877, 116

Waskom M. et al., 2017, seaborn: v0.8.1. Zenodo

West A. A., Weisenburger K. L., Irwin J., Berta-Thompson Z. K., Charbonneau D., Dittmann J., Pineda J. S., 2015, ApJ, 812, 3

Whitelock P. A., Feast M. W., Van Leeuwen F., 2008, MNRAS, 386, 313

Whitelock P. A., Feast M. W., van Loon J. T., Zijlstra A. A., 2003, MNRAS, 342, 86

Wielen R., 1977, A&A, 60, 263

Wilson O., Woolley R., 1970, MNRAS, 148, 463

Wood P. R. et al., 1999, in Le Bertre T., Lebre A., Waelkens C., eds, Proc. IAU Symp. 191, Asymptotic Giant Branch Stars. Kluwer, Dordrecht, p. 151

Wyatt S. P., Cahn J. H., 1983, ApJ, 275, 225

Xiang M. et al., 2017, ApJS, 232, 2

Xiang M., Rix H.-W., 2022, Nature, 603, 599

Yu J., Liu C., 2018, MNRAS, 475, 1093

Zoccali M. et al., 2003, A&A, 399, 931

SUPPORTING INFORMATION

Supplementary data are available at *MNRAS* online.

SupplementaryMaterial.zip

Please note: Oxford University Press is not responsible for the content or functionality of any supporting materials supplied by the authors. Any queries (other than missing material) should be directed to the corresponding author for the article.

This paper has been typeset from a TEX/LATEX file prepared by the author.